Membraneless Microfluidic Fuel Cells

by

Kamil S. Salloum

A Dissertation Presented in Partial Fulfillment
of the Requirements for the Degree
Doctor of Philosophy

Approved November 2010 by the
Graduate Supervisory Committee:

Jonathan D. Posner, Chair
Ronald J. Adrian
Jennifer Blain Christen
Kangping Chen
Patrick E. Phelan

ARIZONA STATE UNIVERSITY

December 2010

ABSTRACT

Portable devices rely on battery systems that contribute largely to the overall device form factor and delay portability due to recharging. Membraneless microfluidic fuel cells are considered as the next generation of portable power sources for their compatibility with higher energy density reactants. Microfluidic fuel cells are potentially cost effective and robust because they use low Reynolds number flow to maintain fuel and oxidant separation instead of ion exchange membranes. However, membraneless fuel cells suffer from poor efficiency due to poor mass transport and Ohmic losses. Current microfluidic fuel cell designs suffer from reactant cross-diffusion and thick boundary layers at the electrode surfaces, which result in a compromise between the cell's power output and fuel utilization.

This dissertation presents novel flow field architectures aimed at alleviating the mass transport limitations. The first architecture provides a reactant interface where the reactant diffusive concentration gradients are aligned with the bulk flow, mitigating reactant mixing through diffusion and thus crossover. This cell also uses porous electro-catalysts to improve electrode mass transport which results in higher extraction of reactant energy. The second architecture uses porous electrodes and an inert conductive electrolyte stream between the reactants to enhance the interfacial electrical conductivity and maintain complete reactant separation. This design is stacked hydrodynamically and electrically, analogous to membrane based systems, providing increased

reactant utilization and power. These fuel cell architectures decouple the fuel cell's power output from its fuel utilization.

The fuel cells are tested over a wide range of conditions including variation of the loads, reactant concentrations, background electrolytes, flow rates, and fuel cell geometries. These experiments show that increasing the fuel cell power output is accomplished by increasing reactant flow rates, electrolyte conductivity, and ionic exchange areas, and by decreasing the spacing between the electrodes. The experimental and theoretical observations presented in this dissertation will aid in the future design and commercialization of a new portable power source, which has the desired attributes of high power output per weight and volume and instant rechargeability.

To my Mother and Father.

I love you both so much.

ACKNOWLEDGMENTS

This dissertation would not have been possible if not for the support of the following individuals:

- My chair and advisor, Dr. Jonathan Posner, whose mentorship and guidance greatly evolved my critical thinking skills and will resonate within me throughout my professional career
- My graduate committee professors, whose engaging discussions, coursework, and suggestions helped shape the progress of this work
- My uncle, Dr. Kamil Kaloush, and my brother, Dr. David Salloum, whose personal and professional advice continue to prove invaluable
- My parents and my sisters Hala and Lilian, for their love, support, and availability during times of need
- Aunt Carmen, Angela, and Andrea, for treating me as part of the family and integrating me into the wonderful American culture
- My friends and colleagues Philip, Steve, Jeff, Juan, Nathan, Michael, Carlos, Charlie, Babak, and Wen Che for all the intellectual discussions and great graduate curricular experience
- Last but not least, my fiancée Kristen, whose patience, love, and support makes a better man out of me every day.

Thank you all.

TABLE OF CONTENTS

Page

LIST OF TABLES

LIST OF FIGURES

CHAPTER 1

Introduction

In this chapter I provide the motivation for portable power sources, the difficulty in achieving it for scaled down membrane based fuel cells, and review existing work on microfluidic fuel cells. I describe the advantages of using liquid reactants and microfluidic architectures in providing compact power for portable power applications. I end this chapter with detailed objectives for this dissertation.

1.1. Motivation

Portable electronic devices have become a part of the modern human's everyday life, yet their ever-growing sophistication is not equally met with their increased power demand [1]. To supply this electrical energy, the majority of portable electronics are powered by rechargeable or disposable batteries, which contribute largely to the overall weight of the system. Table 1.1.1 compares the energy densities of common battery types in use today, at 20% efficiency [1, 2]. It is unsurprising that many modern handheld and portable devices use lithium ion based batteries, since they exhibit higher specific energy densities and reduce the overall weight and volume of the system.

Table 1.1.1:

Practical gravimetric and volumetric energy densities of common batteries

Battery Type	**Gravimetric Energy Density (Wh kg^{-1})**	**Volumetric Energy Density (Wh l^{-1})**
Nickel Cadmium	80	400
Nickel Metal Hydride	120	1000
Lead Acid	50	600
Lithium Cobalt	190	1500

Alternative fuels and their theoretical energy densities are presented in Table 1.1.2. Even at comparable battery operating efficiencies of 20%, these fuels still exhibit higher volumetric and, with the exception of hydrogen, gravimetric energy densities than batteries. Higher energy densities are desirable so power systems can be designed with lesser weight or volume allocation for the power source. Liquid fuels also prompt the concept of a fuel cell; a flow based electrochemical cell where reactants are stored externally and brought to a local reaction zone.

Table 1.1.2:

Theoretical gravimetric and volumetric energy densities of liquid fuels

Fuel	**Gravimetric Energy Density (Wh kg^{-1})**	**Volumetric Energy Density (Wh l^{-1})**
Formic Acid	2086	1710
Methanol	4690	6400
Ethanol	6100	7850
Hydrogen gas (100 bar)	300	39000
Sodium Borohydride	2925	2840
Vanadium[1]	20	25

Fuel cells are just one type of chemical reactors that rely on heterogeneous catalysis to produce power from the energy stored in molecular species[3]. The polymer electrolyte membrane (PEM) hydrogen fuel cell delivers a high energy to weight ratio, non-corrosive, and fast response power system operating at 25 to 80 °C [3]. The cross section of the fuel cell is shown in Figure 1.2.1. Hydrogen gas is oxidized at the catalyst layer of the anode to produce electrons and protons. The electrons are shuttled externally as a current source for electrical devices. The protons are transported through an ion selective, perfluorinated polymer

[1] Despite vanadium's comparably low energy density to the other fuels in this table, it is listed here due to its use in characterizing microfluidic fuel cells in Chapter 3.

membrane which is impermeant to electrons and negatively charged ions. The polymer membrane has nanoscale charged pores that forms overlapping electric double layers and excludes all species transport except for cations. The electrons and protons combine with the oxidant (usually oxygen in air) on the catalyst surface of the cathode to complete its reduction reaction.

The ion exchange membrane is the most critical component to proper operation of the hydrogen fuel cell. The membrane completes the electrochemical circuit and prevents reactant crossover from the anode to the cathode, which would result in both reactions occurring on a single site with no external electron conductance. Several technical challenges are associated with using a polymer membrane. Degradation requires frequent replacement and maintenance of the ion exchange membrane [4-9]. The reduction reaction at the cathode results in water build up which prevents oxidant from reaching the catalyst surface [10-14]. Under higher pressures and temperatures, reactants, particularly liquids, may cross the membrane and result in potential losses due to counter electrode activity [15-17]. The previous complications are generally countered through the use of auxiliary humidification, temperature, and flow control systems which add to the overall cost and complexity of the fuel cell system.

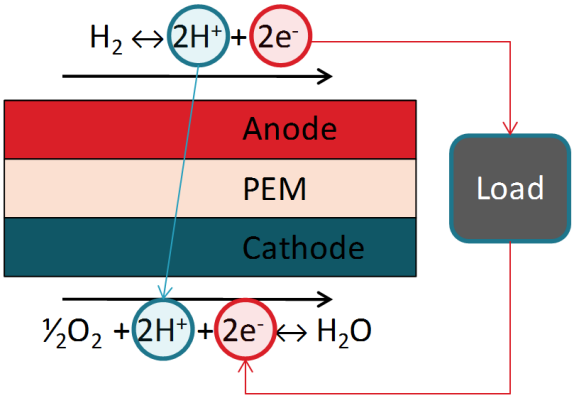

Figure 1.1.1: Schematic showing a standard PEM hydrogen fuel cell cross sectional view.

Miniaturization efforts for fuel cells were first aimed at scaling down PEMFC architecture [18, 19]. Ha et al. and Rice et al. tested a variety of formic acid concentrations with ambient air on a 2 cm × 1.4 cm PEM architecture [20, 21]. Jiang et al. fabricated a 1.1 cm × 1.3 cm direct methanol fuel cell with etched silicon for air breathing and silicone channels for methanol distribution [22]. Yeom et al., Yao et al., and Kamitani et al. directly integrated the membrane electrode assembly (MEA) on micron scale silicon features for use with a variety of fuels [23-25]. While such devices offer a small scale solution, they retain the abovementioned technical challenges associated with a PEM fuel cell.

Another approach is the removal of the semi-permeable polymer membrane by low Reynolds number flows in microscale architectures. The unique advantage of flows in microfluidic devices is the deterministic laminar flows that allow the flow of reactants without significant mixing due to stirring [26-29]. Another advantage is the large surface to volume ratios. Heterogeneous

chemical reactions involve the interaction of a fluid (typically the reactant) and a solid phase [30]. The surface to volume ratio in cylindrical channels scales as D_h^{-1}, where D_h is the hydraulic diameter of the channel. In microfluidics, typical D_h values range from 10^{-3} to 10^{-6} m, which results in large surface to volume ratios and favorable conditions for heterogeneous reactions. The promise of microfluidic fuel cells is high energy density devices that have small form factors, rapid responses to changes in current draw, and can be readily parallelized to provide power for a variety of portable power applications [31].

1.2. Literature review of microfluidic fuel cells

Ferringo et al. [32] introduced the concept of a membraneless microfluidic fuel cell, and Choban et al. [33] characterized the device electrochemically. Figure 1.3.1 shows a schematic of the early design's top view. The microfluidic device is a Y-channel configuration where liquid fuel and oxidant interface directly without the use of a physical membrane. In low Reynolds number regimes, co-flowing parallel streams of liquid fuel and oxidant develop a laminar flow interface [34]. The interfacial area between the two streams resembles a virtual membrane that allows for the exchange of cations (usually protons) transverse to the flow direction from the anode to the cathode. The catalyst is typically located along the entire length of the microchannel sidewalls, with one side acting as anode and the other as cathode.

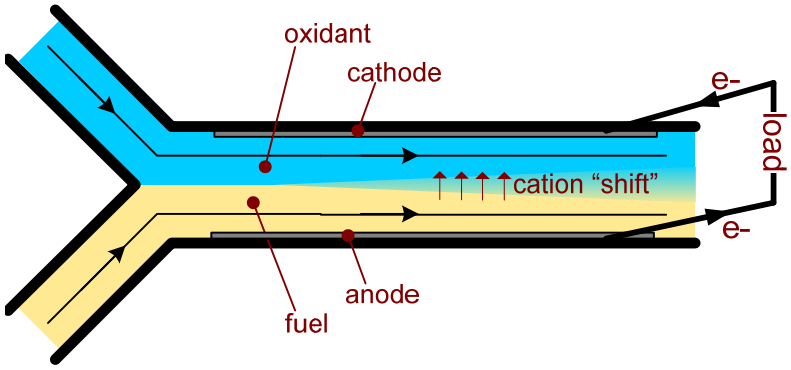

Figure 1.2.1: Schematic showing a planar view of a typical microfluidic membraneless fuel cell.

Membraneless fuel cells offer greater flexibility with fuel and oxidant selection than membrane based cells because they do not have the inherent crossover issues [35]. Membraneless fuel cells have been demonstrated with vanadium [32, 36-38], formic acid [33, 39], hydrogen saturated electrolytes [40-42], gaseous streams [42-44], peroxide [45], methanol [46, 47], ethanol [48], borohydride [49], and have been tested in both basic and acidic media [50-53]. Liquid reactants are preferable from fuel safety, storage, and energy density standpoints [54].

The parallel flow design requires careful consideration of the development of both the viscous and concentration boundary layers, because the flow rates are linked to the power density and fuel utilization [55]. The power density of parallel flow fuel cells increases with increasing flow rate. Higher flow rates generate higher power because they reduce the concentration boundary layer thickness at the electrodes resulting in lower mass transport losses [56]. The

improvements in power density come at the expense of fuel utilization because the fuel and oxidant reach the end of the cell before they are consumed. Since the flow rate and the mass transport at the electrode are tightly coupled, efforts have been made to alter the microchannel geometry to improve the mass transport behavior and cell performance. In earlier developments, Kjeang et al. increased electrocatalyst surface area using sheets or stacks of graphite rods in a vanadium-redox fuel cell in an effort to improve fuel utilization [36, 37], Cohen et al. introduced a planar tapered flow that delays the onset of reactant depletion to reduce wasted reactant [40], and Sun et al. introduced a parallel flowing electrolyte between the reactant streams in order to reduce reactant mixing [41].

Membraneless fuel cells typically exhibit higher Ohmic losses which result in lower power densities than membrane based fuel cells. The increased Ohmic loss is attributed to the increased distance between the anode and cathode, compared to the membrane assembly found in a PEM fuel cell. In parallel flow designs, unreacted fuel and oxidant mix by transverse diffusion at the laminar flow interface, which results in reactant depletion. Mixing of the fuel and oxidant decreases with increasing flow rate because the reactants are advected downstream with greater velocity (higher Peclet number) [56]. Although larger flow rates result in less mixing of the streams at the interface and higher power output from the cell, the fuel and oxidant may reach the end of the cell before they are consumed, resulting in a net reduction in fuel utilization. The concentration boundary layer at the flat electrode surfaces increases in thickness as the reactants

travel downstream, which further increases the mass transport resistance of the fuel or oxidant to the reactive surface.

1.3. Objectives

The primary goals of this dissertation are to answer the questions: *Can the microfluidic fuel cell power density be increased without sacrificing fuel utilization?* and *How does the microfluidic fuel cell's design control its performance?*.

For the first question, I present three membraneless microfluidic fuel cell architectures. I use porous electrodes to increase the reaction surface area and reduce the concentration boundary layer thickness which result in increased current, and therefore power output. I also reduce the diffusive mixing and maintain separation between the two reactants by using an electrolyte flow. Separated streams alleviate complications with reactant depletion and undesirable potential losses associated with the presence of a reactant at its counter electrode. I also successfully recycle reactants to increase the fuel utilization and power output from the fuel cell.

For the second question, I present experiments to understand the effect of geometric variations on the fuel cell's power output and fuel utilization. To do this, I leverage the distinct electrochemical behavior of hydrogen peroxide, as a single reactant, on two different metal surfaces. The motivation behind using a single reactant scheme is to provide a controlled experimental platform where flow field perturbations are reduced. The distance between the two electrodes, the lengths of the electrodes, and the cross sectional area of the ionic interface are

varied to investigate their effect on fuel cell power and fuel utilization. To our best knowledge, a detailed experimental study on the geometric variations of microfluidic fuel cells is not available, and would be a valuable addition to the field.

CHAPTER 2

Background

In this chapter I present the fundamental and governing equations relevant to the microfluidic fuel cell field. In the first section I present fundamental transport phenomena relationships and the isothermal assumption. In the second section I present the governing fluid mechanics and establish the appropriate scaling and equation forms. In the third section I present the fundamental mass transport equations and outline the dominant parameters in microfluidics. In the fourth and last section I integrate electrochemical phenomena and outline thermodynamic irreversablities in fuel cell operation.

2.1. Constitutive equations and assumptions

Constitutive relationships are used to define how the flux, or transport, varies on the spatial gradient of the entity (e.g. mass). Table 2.1.1 describes the fundamental relationships for the main transport phenomena, which are obtained empirically. The proportionality constant in these relationships is an important coefficient in many of the non-dimensional parameters that I will introduce in the following sections.

The work encompassed in this dissertation is under the isothermal assumption, since the enlarged surface to volume scales in microfluidics quickly dissipates any locally generated or input heat fluxes. Therefore, the fuel cell is always in thermal equilibrium with the surrounding environment, and all experimental data, unless otherwise noted, are at room temperature.

Table 2.1.1:

Fundamental transport phenomena

Relationship (entity)	**Expression**	**Coefficient**
Fick's Law (mass)	$\vec{J} = -D\nabla C$	Diffusivity
Newton's Law (momentum)	$\tau = -\mu\nabla u$	Viscosity
Fourier's Law (temperature)	$q'' = -k\nabla T$	Thermal Conductivity
Ohm's Law (potential)	$i = -\sigma\nabla V$	Electrical Conductivity

2.2. Hydrodynamics

In fluid mechanics two main expressions define the governing physics of the flow field. The first one is conservation of mass (also known as the continuity relationship), which states that the mass of a closed system is constant. In differential form, this is described through

$$\nabla \cdot \rho\vec{U} + \frac{\partial \rho}{\partial t} = 0, \tag{2.2.1}$$

where ρ is the density of the fluid, $\vec{U}$ is the velocity field, and t is time. For steady and incompressible flows, the density is time and spatially invariant therefore the continuity relationship reduces to

$$\nabla \cdot \vec{U} = 0. \tag{2.2.2}$$

Mathematically, equation (2.2.2) describes that the divergence of the velocity field is zero, which is true when the fluid domain does not contain any sinks or holes.

The second governing expression is the conservation of momentum. By balancing stresses from the translational, rotational, angular deformation, and linear deformation modes of fluid motion, and external body forces on a fluidic element in accordance with Newton's second law, the expression takes the form

$$\rho\left(\frac{\partial\vec{U}}{\partial t}+\left(\vec{U}\cdot\nabla\right)\vec{U}\right)=\nabla\cdot\mathrm{T}+\vec{b}, \tag{2.2.3}$$

where T and $\vec{b}$ are respectively the deviatoric stress tensor and applied external body forces. Equation (2.2.3) is termed the Navier-Stokes equation. For an incompressible and Newtonian fluid, the divergence of the deviatoric stress tensor reduces to $-\nabla p+\mu\nabla^2\vec{U}$ and equation (2.2.3) is rewritten as

$$\rho\left(\frac{\partial\vec{U}}{\partial t}+\left(\vec{U}\cdot\nabla\right)\vec{U}\right)=-\nabla p+\mu\nabla^2\vec{U}+\vec{b}, \tag{2.2.4}$$

where p is the fluid pressure and $\vec{b}$ is the external applied force [57]. For application in microfluidics, I non-dimensionalize equation (2.2.4) according to the variables

$$\left(x^*,y^*,z^*\right)=\frac{(x,y,z)}{L},\ t^*=\frac{tU}{L},\ \left(u^*,v^*,w^*\right)=\frac{(u,v,w)}{U},\ \text{and}\ p^*=\frac{\left(p-p_\infty\right)L}{\mu U}.$$

Here L is a characteristic length scale, U is a characteristic velocity, and p_∞ is a reference pressure for the system. For small length scales viscous forces are dominant and hence the dimensionless pressure is scaled accordingly. Substituting the above variables into equation (2.2.4), and neglecting external body forces, I arrive at the following form of the Navier-Stokes equation:

$$\mathrm{Re}\left(\frac{\partial \overrightarrow{U^*}}{\partial t^*}+\left(\overrightarrow{U^*}\cdot\nabla^*\right)\overrightarrow{U^*}\right)=-\nabla^* p+\nabla^{*2}\overrightarrow{U^*}\,. \tag{2.2.5}$$

Re is the Reynolds number defined as $Re=\rho UL/\mu$. The Reynolds is a ratio of the inertial to the viscous forces, and in the microfluidic regime this limit is $Re<1$. Dropping the left hand side terms in equation (2.2.5) and redimensioning the remaining variables results in the creeping flow equation:

$$\nabla p=\nabla^2\vec{U}\,. \tag{2.2.6}$$

An example problem in microfluidics is isothermal flow through a cylindrical capillary with radius *a*, shown in Figure 2.2.1. At the wall ($r=a$), a no-slip (zero velocity) condition applies. The remaining boundary condition can be determined through symmetry at the centerline ($r=0$), or equivalently, a finite velocity value at the centerline.

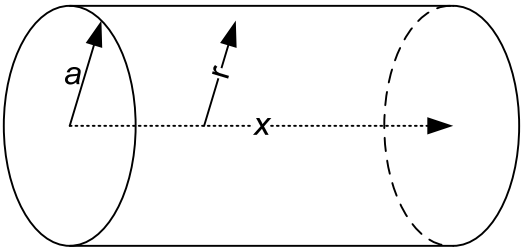

Figure 2.2.1: Microfluidic capillary aligned along the *x* axis with radius $r=a$.

Solving equation (2.2.6) assuming azimuthal and longitudinal symmetry with pressure gradients only in the *x* direction leads to

$$u(r)=-\frac{a^2}{4\mu}\frac{dp}{dx}\left(1-\frac{r^2}{a^2}\right). \tag{2.2.7}$$

A useful derivation can be obtained from equation (2.2.7). Define the flow rate Q in the channel as the average velocity through the cross-sectional area

$$Q = \int_0^{2\pi} \left(\int_0^a u(r) r dr \right) d\theta . \tag{2.2.8}$$

After integration, the resulting expression relates the flow rate and pressure to the channel geometry as

$$Q = -\frac{\pi}{8\mu} \frac{dp}{dx} a^4 . \tag{2.2.9}$$

Equation (2.2.9) states that the pressure gradient to sustain a flow rate Q scales with a^{-4}. Since microfluidic fuel cells benefit from increased surface areas through porous media, as discussed later, this particular scaling and other derivations from the Navier-Stokes equations become an important tool in optimizing the flow and reaction coupling.

2.3. Species advection, diffusion, and reaction

A similar differential approach from the previous section can be applied to the conservation of a species of mass,

$$\dot{m}_{i,in} - \dot{m}_{i,out} + \dot{m}_{i,generated} = \dot{m}_{i,stored} , \tag{2.3.1}$$

where the subscript i refers to a particular species, and $\dot{m}$ is species rate of change with respect to time. Assuming a single species for simplicity, the differential form of this conservation law is

$$\frac{\partial C}{\partial t} + \nabla \cdot \left(\vec{J}_T \right) = R . \tag{2.3.2}$$

Here C is the concentration of the species, R is the reaction rate into the domain, and $\vec{J}_T$ is the total flux encompassing all applicable flux contributions. For

example, in the absence of a potential field, or with a neutrally charged species, and for a dilute species the only flux contributions are diffusive and convective such that

$$\vec{J}_T = \vec{U}C - D\nabla C\,, \tag{2.3.3}$$

where D is the binary diffusion coefficient of the species in its solvent [58]. Substituting equation (2.3.3) into equation (2.3.2) and rearranging leads to

$$\frac{\partial C}{\partial t} + \vec{U}\cdot\nabla C = D\nabla^2 C + R\,. \tag{2.3.4}$$

To compare the relative terms in equation (2.3.4), ignore the reaction term and non-dimensionalize using the following variables

$$\left(x^*, y^*, z^*\right) = \frac{(x, y, z)}{L},\ t^* = \frac{tU}{L},\ \left(u^*, v^*, w^*\right) = \frac{(u, v, w)}{U},\ \text{and}\ C^* = \frac{C}{C_\infty},$$

where C_∞ is a reference (typically bulk) species concentration. The equation in non-dimensional form is

$$\frac{\partial C^*}{\partial t^*} + \vec{U}^*\cdot\nabla^* C^* = \frac{1}{Pe}\nabla^{*2} C^*, \tag{2.3.5}$$

where Pe is the Peclet number defined as $Pe=UL/D$. The Peclet number is the ratio of advective to diffusive transport. Typically, for dilute and aqueous solutes, $Pe>>1$, which scales the diffusive term on the right hand side negligible with the convective and time varying terms. An applied example and similar derivation of equation (2.3.5) is presented in Chapter 4, Section 3.

2.4. Fuel cells and electrochemistry

Fuel cells couple the transport of momentum, mass, and charge to convert chemical energy to electrical energy. As with any thermodynamic system, fuel cells suffer from various irreversibilities that arise from each transport process. These irreversibilities are reflected in the fuel cell's performance as a reduction in the reversible potential, defined as

$$V_r = \frac{-\Delta g}{nF}, \tag{2.4.1}$$

where Δg is the change in Gibbs free energy resulting from the distinct chemical reactions in each half cell, F is Faraday's constant, and n is the number of electrons transferred. The potential according to equation (2.4.1) decreases in four consecutive modes when the fuel cell is sourcing current. For the purposes of this dissertation, the total of the potential losses is termed the fuel cell polarization. Polarization is graphically depicted by plotting the respective fuel cell potential at each current density. The following segments describe each polarization loss individually

At the onset of current density, a potential drop due to activation losses occurs. These losses are due to potentials required to transfer charge from the chemical phase to the electrode surface. In other words, activation losses reflect electrode kinetic limitations in the fuel cell. Potential losses due to activation can be stated as

$$V_{act.} = a \ln\left(\frac{i}{i_o}\right), \tag{2.4.2}$$

where a is the Tafel slope, i is the fuel cell's current density, and i_o is the exchange, or equilibrium, current density specific to the electrode and reactant. The Tafel slope is a constant that increases with slower, electron transfer limited reactions. The Tafel slope is obtained experimentally through measuring the current density of oxidation and reduction through an electrode in the reactant solution. Its kinetics can be described through the Butler-Volmer equation

$$i = i_0 \left[\exp\left(-\frac{\alpha n F \left(V - V^o \right)}{RT} \right) - \exp\left(\frac{\left(1-\alpha\right) n F \left(V - V^o \right)}{RT} \right) \right]. \tag{2.4.3}$$

At large values of $V - V^o$ equation (2.4.3) reduces to equation (2.4.2) and therefore the magnitude of the slope a is

$$a = \frac{\alpha n F}{RT}, \tag{2.4.4}$$

where α is a symmetry coefficient that describes the relative energy barrier required for a charge to cross from the solution to the electrode, and vice versa. The potential V^o is the reversible potential for the unique half cell reaction under consideration. Therefore, i_o is different for oxidation and reduction and the fuel cell is therefore limited by the slower reaction. Activation losses are material specific since they are dependent on surface properties, catalyst structure and loading, and reactant adsorption [3].

At moderate current densities, potential losses due to the resistance of the fuel cell develop. These potential drops are termed the Ohmic losses and are due to the in series resistance of the electrode, connections, as well as the resistance to

the flow of redox ions within the reactive media. If the sum of all resistances in the fuel cell is equivalent to R, then Ohmic losses are interpreted as

$$V_{Ohmic} = iR\,. \tag{2.4.5}$$

Ohmic losses depend on the conductivity of all charge and electron carrying media in the fuel cell, shown in Chapter 3, and the geometry of the fuel cell's construction, which is discussed in detail in Chapter 4.

At higher current densities, the fuel cell undergoes a mass transport limitation, where the rate of chemical conversion is much greater than the rate of chemical delivery at the catalyst surface. Physically, the rapid consumption of reactant at the electrode results in a reactant concentration polarization between the bulk fluid and catalyst sites. This region is known as the concentration boundary layer. For a flat plate electrode, the boundary layer has been calculated by Blasius [56] through a similarity solution of the Navier-Stokes equations coupled with the advection diffusion equation as

$$\delta_c = \frac{5x}{Sc^{1/3} Re_x^{1/2}}, \tag{2.4.6}$$

where x is a downstream distance from the entrance of the electrode, and Sc is the Schmidt number, the ratio of viscous and diffusion coefficients. While it is difficult to analytically identify potential losses due to mass transport, an acceptable approach is to empirically obtain a proper fit to the following expression:

$$V_{mass} = m\exp(ni)\,, \tag{2.4.7}$$

where m and n are constants pertinent to a unique fuel cell system [3].

Combining the abovementioned losses leads to the fuel cell potential as a function of current density

$$V = V_r - V_{act.} - V_{Ohmic} - V_{mass} = V_r - a\ln\frac{i}{i_o} - iR - m\exp(ni)\,. \tag{2.4.8}$$

Figure 2.4.1 illustrates a typical fuel cell polarization curve with the three losses identified. The objective of any fuel cell designer is to reduce any drastic effects from these losses, whether from a materials science, construction, chemical, or hydrodynamic approach.

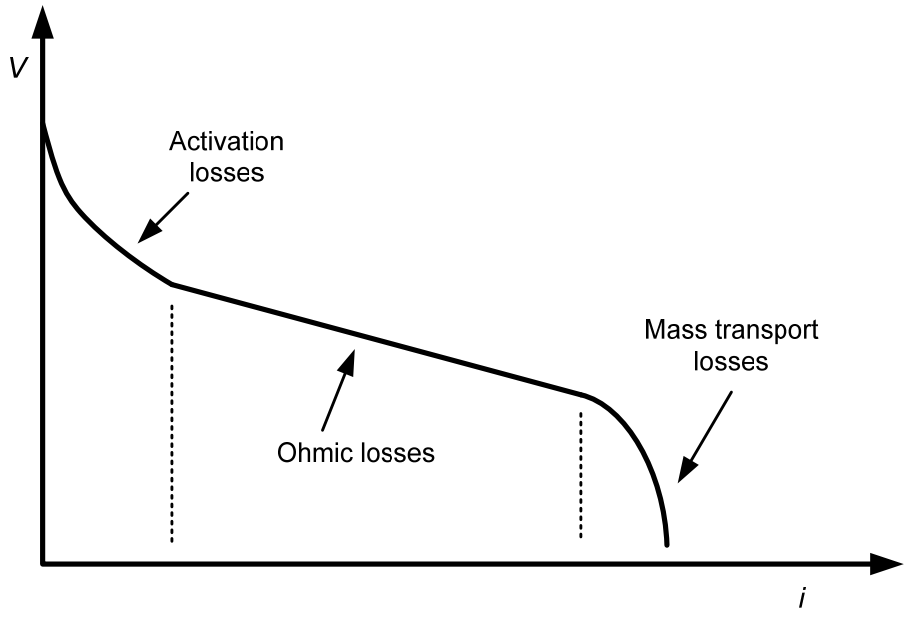

Figure 2.4.1: Typical fuel cell polarization curve with activation, Ohmic, and mass transport loss regions indicated.

CHAPTER 3

Novel Microfluidic Fuel Cell Architectures

This chapter details contributions to the microfluidic fuel cell field that alleviate the complications of parallel flow architectures. Section 3.1 describes a microfluidic fuel cell where reactants flow in series through radial porous electrodes [39]; the sequential flow reduces broadband diffusion between the two streams by aligning the diffusion gradient with, and not transverse to, the bulk flow of the streams. The radial expansion in the architecture increases the in plane ion exchange surface area and electrode surface area. The effects of reactant flow rates and their supporting electrolyte concentrations are described. Section 3.2 describes a microfluidic fuel cell where an electrolyte maintains constant separation between the two reactants; to overcome complications with reactant mixing, an electrolyte flow rate as low as 5% of the reactant flow rates separates the reactants at the ionic interface and throughout their residence time in the fuel cell. The flow rate of the separating electrolyte and its effect on the fuel cell performance is presented [59]. Section 3.3 combines the lessons learned from the prior two architectures; the use of porous electrodes, the reduction of diffusive mixing, and the increase of ionic exchange and reaction surface area. The architecture consists of two separating electrolyte interfaces in series [60]. The influence of the first cell's electrochemical state on the second cell is characterized.

3.1. Sequential Flow Fuel Cell

3.1.1. Motivation

In parallel flow designs, transverse diffusion of fuel and oxidant at the laminar interface results in reactant depletion. Flat plate electrodes also result in increasing concentration boundary layer thickness as the reactants travel downstream. Thick boundary layers reduce fuel cell power by decreasing the concentration gradient at the electrode wall, which results in poor mass transport to the surface. In this section I present a membraneless fuel cell where the fuel and oxidant flow in series through radial porous electrodes. The sequential flow reduces transverse diffusion between the reactant streams by aligning the diffusion gradient at the interface along bulk flow of the streams. The radial expansion in the architecture increases the in plane ion exchange surface area and electrode surface area.

Figure 3.1.1 shows a schematic of the sequential flow membraneless fuel cell with porous disk electrodes. The fuel stream is introduced at the center of the anode and flows radially outwards through a porous disk electrode with diameter D_a and height h. As the fuel flows radially outward, it is oxidized on platinum nanoparticles coating the surface of the porous electrode. Electrons are conducted through an external circuit and react with the oxidant at the cathode. Ideally, all the fuel is completely oxidized before exiting the anode which may alleviate issues related to mixing of unreacted fuel and oxidant. The oxidant is introduced in series with the fuel, at a location radially outward from the anode, approximately $r = D_a/2 + g$. The oxidant and oxidized fuel combine and flow

towards an annular disk porous cathode with width $D_{c2} - D_{c1}$ and height h. The oxidant is reduced at the cathode, complexes with the oxidized fuel, and continues to flow outward away from the cathode towards an azimuthally distributed waste outlet. The oxidant stream should not reach the anode so to avoid mixed potentials. The gap between the anode and cathode serves as an electronic insulator between the anode and cathode as well as separates the fuel and oxidant under the defined flow field. The oxidant will not reach the anode as long as the flows are laminar and stable, and the radial convective velocity at the interface between the two streams is greater than the characteristic speed of diffusion of the oxidant (as described later in the discussion).

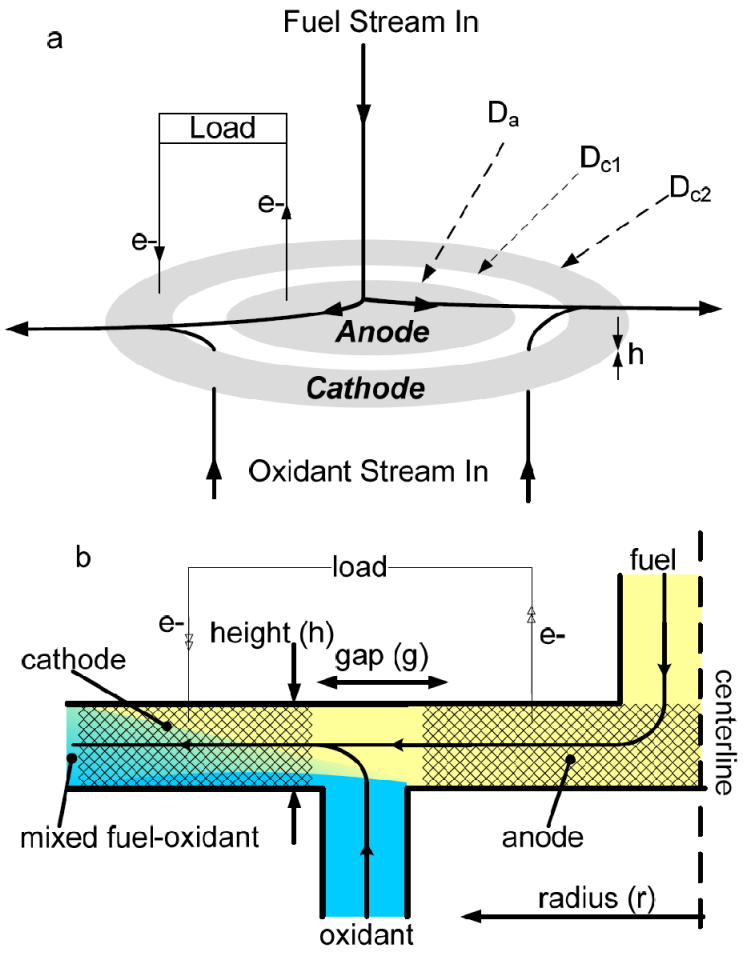

Figure 3.1.1: Schematics of electrode design and flow paths of the radial membraneless fuel cell as (a) isometric projection and (b) cross section.

This sequential flow configuration improves mass transport by advecting the reactants through porous electrodes and waste products downstream. In addition, the streams are not flowing in parallel thereby avoiding a diffuse interface along the length of the cell. Using the current cell design, it may be possible to completely oxidize the fuel and reduce the oxidant so that the two reactants will not mix and result in mixed potentials and poor fuel utilization.

This fuel cell architecture allows for tuning of the electrode surface areas as well as the independent control of the fuel and oxidant flow rates. This paper presents a radial flow fuel cell that is constructed of bulk machined polymethyl methacrylate (PMMA), carbon paper electrodes, and Pt black catalyst. The fuel used is formic acid in sulfuric acid. The oxidant is potassium permanganate in sulfuric acid. Using particle image velocimetry, I show that the fluid flow field in the fuel cell is radially outward and axisymmetric. I characterize cell performance as a function of the fuel and oxidant flow rate as well as the electrolyte concentration.

3.1.2. Fuel cell construction

Figure 3.1.2 represents a scaled solid model of the radial fuel cell housing. The cell consists of a top and bottom milled PMMA plate, sandwiched by machined 316 stainless steel disks. The steel disks have a radial bolt-hole pattern that acts as a super structure to maintain conformal contact over the entire cell surface. A mixture of formic acid and sulfuric acid (throughout called the fuel) flows through a 1.58 mm hole drilled in the 6.35 mm thick top plate. The fuel is oxidized as it flows through the anode, across the gap and into the cathode. A mixture of potassium permanganate and sulfuric acid (oxidant) is introduced concentrically through a ring of inlets in the approximately 2 mm wide gap and mixes with the oxidized fuel as it flows to the cathode. The waste products are routed out of the cell through concentric outlets placed at $r = 18.5$ mm. A third PMMA plate distributes the waste products. PEEK liquid chromatography ports (N-333, Upchurch Scientific, Oak Harbor, WA) were used to deliver liquid

reactants to the fuel cell. The ports were bonded to the PMMA structures by curing the supplied adhesive rings at 92 °C for 15 hours. Fluorosilicone flat polymer rings with an uncompressed thickness of 400 μm were cut using a laser ablation system (Universal Laser Systems, Scottsdale, AZ) and served as support for the concentric catalyst structures.

The electrodes are fabricated from Toray carbon paper (E-TEK, Somerset, NJ) and platinum black (HiSPEC™ 1000, Alfa Aesar, Ward Hill, MA). The anode is 5.1 mm in radius and approximately 100 μm thick. The cathode annulus has an inner radius of 7.0 mm and an outer radius of 12.7 mm. Figure 3.1.1a shows the electrode shapes with anode and cathode projected surface areas of 0.8 and 3.5 cm^2, respectively. Electrocatalysts were prepared by mixing 5 mg Pt black in isopropyl alcohol (CAS 67630, Fisher Scientific, Waltham, MA) and evaporating the alcohol onto the Toray paper, leaving the Pt residue. The Pt coated paper was placed under vacuum overnight to remove residual alcohol. Current was collected with a 0.127 mm platinum wire placed in contact with the electrode and sandwiched by the gaskets.

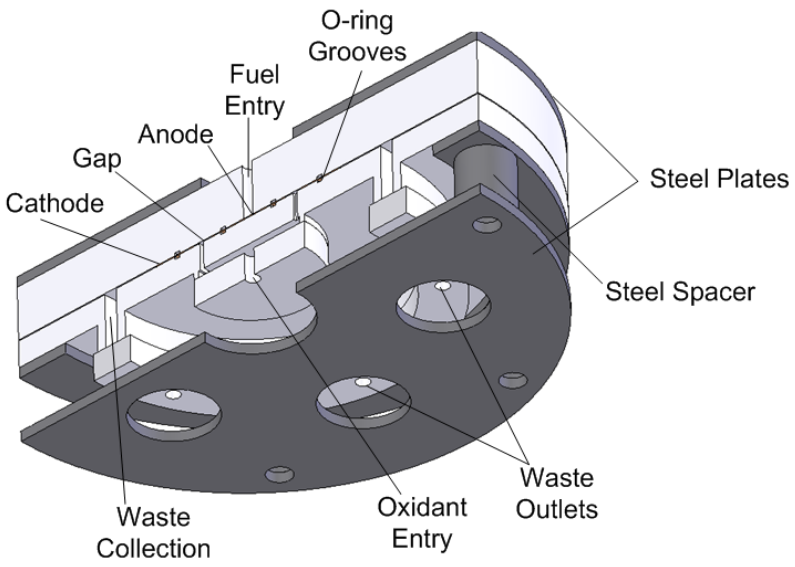

Figure 3.1.2: Scaled cross section of assembled radial flow fuel cell.

The reactants were delivered to the fuel cell by two independent programmable syringe pumps (KDS200, KD Scientific, Holliston, MA). The fuel cell leads were connected to a source meter (Model 2410, Keithley Instruments, Cleveland, OH) operating in galvanostatic mode. Galvanostatic measurements were taken in steps of 0.2 or 0.5 mA, starting from open circuit potential. The current and voltage were collected using a PC and Labview (National Instruments, Austin, TX) connected to the source meter via GPIB interface. After each change in the current, the cell requires 10 to 15 seconds to reach a steady state voltage. The voltages reported here are time averaged over 30 seconds after the transient response.

For the flow characterization experiments, I use microscale particle image velocimetry (μPIV) to track the flow velocity in the cell. μPIV infers the fluid

flow velocity by tracking the displacement of particle flow tracers over two instantaneous images [61, 62]. The flow tracers used are 5 μm fluorescent polystyrene microspheres (G0500, Duke Scientific, Fremont, CA) diluted in DI water. The particle motion is imaged using an inverted epifluorescence microscope (TE2000U, Nikon, Tokyo, Japan), 1X, 0.10 NA objective, and a cooled 16 Bit CCD camera (Cascade 512IIB, Roper Scientific, Tucson, AZ). The low numerical aperture objective results in fluid measurements that are depth averaged across the height of the cell. Captured flow images were cross correlated and validated using PIV Sleuth (Laboratory for Turbulent and Complex Flow, UIUC). The time between exposures was 168.5 msec with an average particle displacement of 10 pixels. The cross correlations were calculated using interrogation windows of 32x32 pixels and 50% overlap. The displacements are determined using a 9 point based Gaussian interpolation of the correlation maps. The fluid velocity vector fields reported are validated using an eight neighbor magnitude comparison and an average of 10 image pairs.

3.1.3. Chemistry

Reactants were prepared by mixing in the supporting electrolyte of 0.5 or 1 M sulfuric acid (CAS 7664939, EMD Chemicals, Hibbstown, NJ) in 18.3 MΩ deionized water (Millipore, Billerica, MA). The fuel and oxidant are formic acid (CAS 64186, Sigma Aldrich, St. Louis, MO) and potassium permanganate (CAS 7722647, Sigma Aldrich, St. Louis, MO), respectively. The electrochemical reaction at the anode is [63]

$$HCOOH \leftrightarrow CO_2 + 2H^+ + 2e^- \quad (E^o = -0.199 \text{ V vs. SHE}), \tag{3.1.1}$$

The anodic reaction involves the production of carbon dioxide. Carbon dioxide is soluble in aqueous solvents, at standard room temperature and pressure, up to a mole fraction of approximately $6x10^{-4}$ [63], equivalent to 33 mM. At the largest currents tested (23 mA), the CO_2 generation rate is $1.2x10^{-7}$ moles/s. At a flow rate of 5000 µl/min I expect a dissolved CO_2 molarity of 1.44 mM. This molarity is well within the solubility limits of CO_2 gas in aqueous solutions. Therefore, there is no carbon dioxide bubble nucleation in the solution.

Although there are various routes for permanganate reduction, the primary permanganate reduction at the cathode is in an acidic medium and is given by

$$MnO_4^- + 8H^+ + 5e^- \leftrightarrow Mn^{2+} + 4H_2O \quad (E^o = 1.507 \text{ V vs. SHE}). \tag{3.1.2}$$

In the presence of the permanganate ion, Mn(II) is oxidized in acid media and produces the insoluble MnO_2 through the reaction [64]

$$2MnO_4^- + 3Mn^{2+} + 2H_2O \leftrightarrow 5MnO_{2(s)} + 4H^+ \quad (E^o = 0.46 \text{ V vs. SHE}). \tag{3.1.3}$$

The maximum theoretical open circuit potential is predicted as 1.706 V, assuming all reactants are completely oxidized or reduced, but this may be lowered by the secondary reaction given in (3.1.3).

I investigated a variety of experimental conditions, including: the supporting electrolyte concentration; the oxidant and fuel flow rates; and the fuel-oxidant flow rate ratio. Table 3.1.1 shows a summary of the experimental parameters. The permanganate concentration was fixed at 10 mM because at higher concentrations MnO_2 precipitates (see equation 3.1.3) and settles in the

pores of the cathode carbon paper occluding fluid flow in the cell. The formic acid concentration was fixed at 40 mM to remain within the stoichiometric range of the net reaction. The maximum flow rate was 5 ml min^{-1}, as the cell leaks at higher flow rates due to the pressure required to sustain the flow. The sulfuric acid concentration was investigated at 0.5 and 1 M.

Table 3.1.1:

Summary of experimental parameters for the radial flow fuel cell.

Parameter	**Range**
Flow Rate	100-5000 µl min^{-1}
Supporting Electrolyte Concentration	0.5 &1 M
Oxidant Concentration	1-100 mM
Fuel Concentration	3-40 mM
Fuel:Oxidant Flow Rate Ratios	1 & 2

3.1.4. Results and analysis

Here I present the results and analysis of the flow field measurements and electrochemical characterization of the radial flow fuel cell. Fuel cell polarization curves, power density, resistance, and fuel utilization are reported as a function of the flow rates and electrolyte concentration.

Characterization of the flow field

The architecture of the radial flow fuel cell requires that the reactants flow uniformly toward the cathode. It is especially critical that the oxidant stream not reach the anode or mixed electrochemical potentials may be observed. I

quantitatively measure the fluid velocity in the cell using μPIV. For these flow measurements, a 2.5 mm radius anode (smaller than that of the active cell) was used to increase the visible area in the gap. The vector field for fuel and oxidant flow rates of 500 μl min^{-1} is presented in Figure 3.1.3a. Qualitatively, the vector field reveals a velocity distribution that spans radially out towards the cathode. The vector field is relatively symmetric in the azimuthal direction, with preferential fluid drift to the left side of the cell in the figure. I attribute the drift to the left side to reduced fluidic resistance due to larger height which is controlled by compression of the o-rings and carbon paper by the bolted super structure.

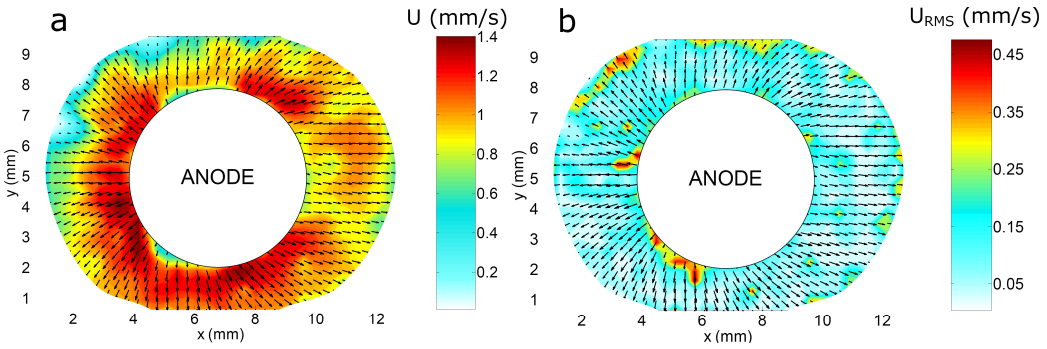

Figure 3.1.3: Contours of (a) average velocity field and (b) velocity root mean square in the radial flow fuel cell. Vector field depicts the average velocity.

Since it is difficult to determine the height of the cell when fully constructed, I can estimate the effective height from the velocity field. Using mass conservation I can infer the effective hydraulic height of the cell using the depth averaged velocity measurement. The effective height is expressed as

$h=Q/2\pi rV(r)$, where Q is the supplied flow rate of the fuel, r is the radial location of the measured velocity, and $V(r)$ is the flow velocity at r. Extracting a sample velocity of 1.0 mm s^{-1} at a radius of 4.0 mm from Figure 3.1.3a (directly to the right of the anode), the effective height is calculated at 332 µm. Given that the Toray paper is approximately 100 µm thick, this implies that the gaskets were compressed from approximately 800 µm to 230 µm. A small effective height is desirable for the radial flow field as a smaller channel height provides viscous damping of the flow at the top and bottom walls similar to a Hele-Shaw flow [57]. The small height increases hydraulic resistance, thus isolating the flow between the electrodes from outside pressure perturbations.

Figure 3.1.3b presents the calculated root mean square (RMS) map of the 10 velocity fields. The RMS velocity was calculated as [65]

$$\boldsymbol{u}_{RMS}(x,y) = \sqrt{\frac{\sum_{i=1}^{n}\left(\overline{\boldsymbol{U}}(x,y) - \boldsymbol{u}_i(x,y)\right)^2}{n}}, \tag{3.1.4}$$

where $\boldsymbol{u}(x,y)$ is the instantaneous velocity vector obtained from image pair i, $\overline{\boldsymbol{U}}$ is the average velocity vector across n image pairs, and quantities in bold are vectors. The computation was performed for both the x and y velocities over 10 image pairs, and the root of the sum of their squares was taken to produce the RMS map. The RMS map shows relatively low RMS values across the flow field, which indicates a steady flow. Toward the left side of the anode, regions of elevated RMS indicate some temporal flow variations. I inject 100 mM fluorescein (CAS 518478, Fisher Scientific, Waltham, MA) into the cathode stream to visualize the path of the oxidant and the interface between the flow from

fuel and oxidant. The cathodic stream does not perturb the anode flow enough to result in cathode fluorescein reaching the anode region. I obtain a steady interface between the cathodic and anodic flow with flow rate ratios (fuel:oxidant) as low as 0.5.

Fuel cell performance

Here I describe the variation of the fuel cell performance on the flow rate of the fuel and oxidant, the flow rate ratio, and the concentration of the supporting electrolyte. The reaction residence times, reaction product advection, and transport due to diffusion at the fuel/oxidant interface are all dependent on the flow rates of the fuel and oxidant. In addition, the supporting electrolyte is a critical parameter in governing Ohmic losses in the cell, as described later.

Figure 3.1.4 presents polarization (a) and power density (b) data for the radial membraneless fuel cell with various flow rates and supporting electrolyte concentrations. The flow rate ratios remain constant at 1:1. Here I report the current density and power density scaled by the fuel cell's total top projected electrode area (4.3 cm^2). The area selection for this cell design is not straightforward and varies over a large range. For example, it is reasonable to choose the anode or cathode areas of 0.8 or 3.5 cm^2, respectively, or their sum. Alternatively the total area that the protons are transported through (~ 0.04 cm^2 at the edge of the anode) may be used. These areas vary by 2 orders of magnitude which may disguise the true performance of the cell. Alternatively, the volume of the cell (~6.5 cm^3) could be used, giving a volumetric power density which may be more appropriate for portable electronic applications. I chose total combined

anode and cathode area for scaling of the current and power densities since it is the largest possible area.

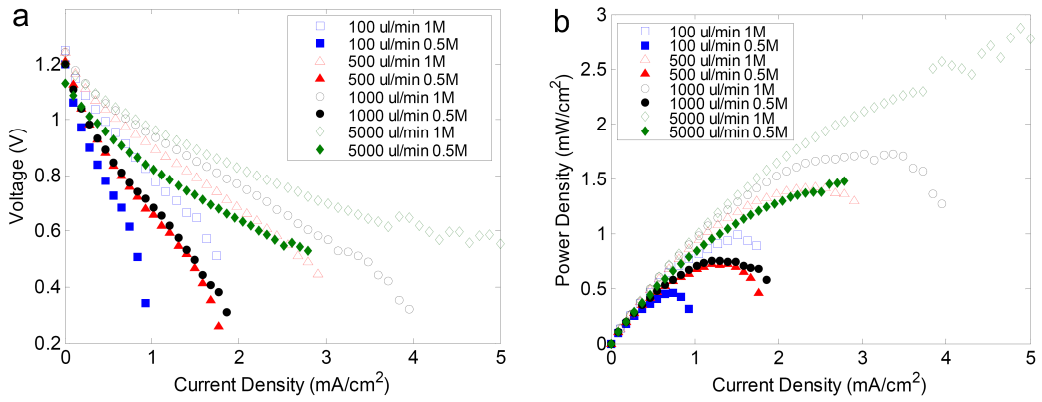

Figure 3.1.4: Polarization (a) and power density (b) curves for the radial fuel cell showing the effect of different reactant flow rates and supporting electrolyte concentration.

In general the polarization curves show cell performance which is similar to other membrane [3] and membraneless [33] fuel cells. I observe an average open circuit potential of 1.2 V. There is an initial decrease in the voltage due to polarization losses at the electrode surface followed by a region of nearly linear variation in the cell potential with current. The slope of the Ohmic region depends on both the concentration of the supporting electrolyte and the flow rate. At higher current densities and some operating conditions, I observe potential drops due to concentration polarization.

Dependence on flow rate

Figure 3.1.4a shows that the cell potential increases with flow rate (1:1 ratio of fuel and oxidant) at a given current load. This trend has been observed in

parallel flow membraneless fuel cells [36]. Higher flow rates not only reduce concentration boundary layer thicknesses, but also increase the turnover rate of the catalyst by removing adsorbed carbon monoxide due to the indirect oxidation (dehydration pathway) of formic acid [21]. At the cathode, I expect that higher flow rates will also reduce fouling from precipitated MnO_2. The maximum flow rate that was explored in the cell was 5 ml min^{-1}.

Figure 3.1.5 shows the polarization (a) and power density (b) data for the cell at flow rate ratios of 1:1 and 2:1 (fuel:oxidant). It is apparent that a decrease in oxidant flow lowers the cell power. Both 1:1 and 2:1 ratios exhibit improved performance with flow rate. As the formic acid is oxidized, the potassium permanganate consumes protons from the background sulfuric acid based on the stoichiometry of the net reaction. However, when permanganate flow rate is decreased (analogous to a rich stoichiometry), the fuel oxidation is limited due to the decreased availability of oxidant at the cathode. As a result, unoxidized fuel flows out of the anode, reacts with the permanganate ions in the gap and further depletes the oxidant. At 5 ml min^{-1} the performance of the cell is nearly identical at the two ratios, suggesting that the above limitations are overcome by the enhanced mass transport at the higher flow rates. Moreover, I observe a small increase in the open circuit potential of approximately 100 mV for the 1:1 flow rate ratio.

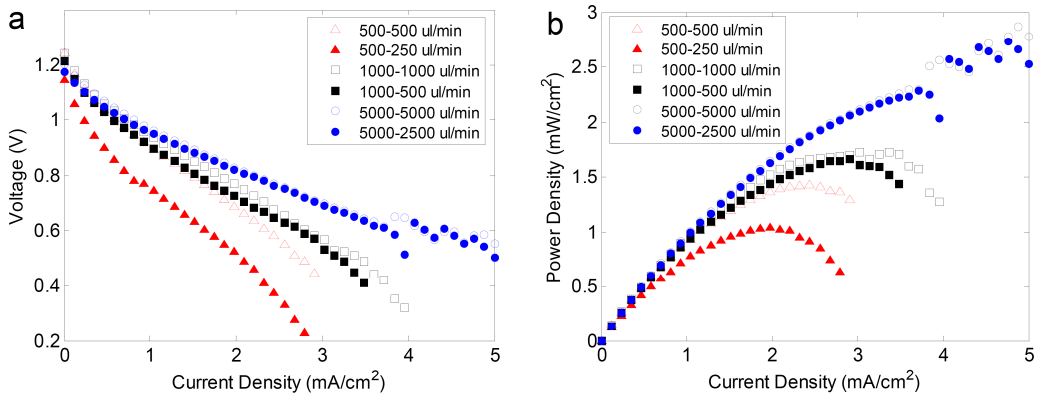

Figure 3.1.5: Polarization (a) and power density (b) curves for the radial flow fuel cell showing the effect of altering the reactant flow rate ratio.

Figure 3.1.6a shows the cell potential versus flow rate (1:1) for several imposed current loads. In general, the cell potential increases with flow rate for a given load. At low flow rates <1000 μL min^{-1}, the potential increases steeply with flow rate. Note that this increase is more prominent at larger currents suggesting that mass transport losses are critical at higher loads. At larger flow rates, the potential is weakly dependent on the flow rate. I attribute this to improvements in mass transport and subsequent extension of the Ohmic loss regime. For example, Figure 3.1.4a shows that at 100 μL min^{-1} there are significant mass transport losses starting at 1.15 mA cm^{-2}. At flow rates in excess of 1000 μL min^{-1}, the polarization curves are linear at the same load and the mass transport losses are not apparent up to 2.8 mA cm^{-2}.

Figure 3.1.6b shows the maximum fuel cell power as a function of the flow rate for two values of the supporting electrolyte concentration and a flow rate ratio of 1:1. I see that the power of the cell also increases with flow rate.

Contrary to the cell potential, the maximum power has a weak dependence on the flow rate for low flow rates (<500 μL min^{-1}) and increases rapidly for higher flow rates. Again, this is due to improved mass transport in the electrodes and extension of the Ohmic regime to higher current densities. Although it appears that increasing the flow rate will continue to increase the cell power, the maximum flow rate is limited by the cell construction and will also result in poor fuel utilization, as discussed later.

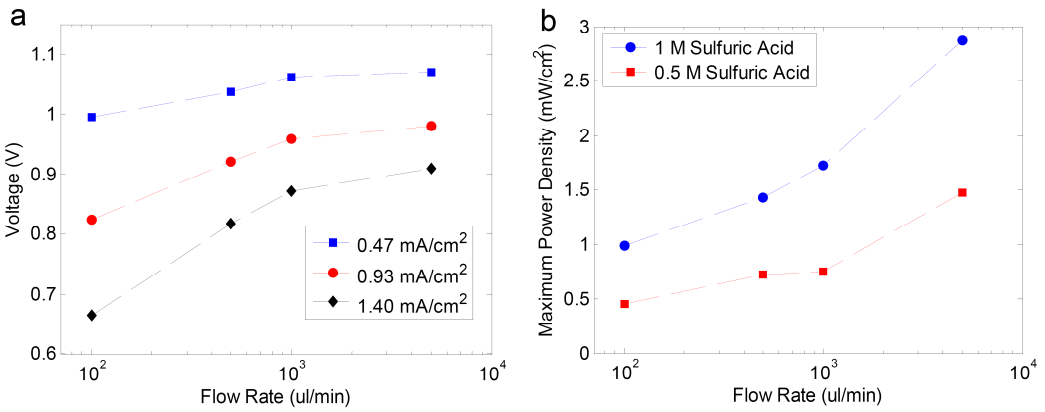

Figure 3.1.6: Radial flow fuel cell potential (a) at different current densities and peak power density (b) at different supporting electrolyte concentrations plotted against flow rate.

Effect of supporting electrolyte concentration

In a membraneless fuel cell, the supporting electrolyte provides an electrochemical bridge from the anode to the cathode similar to the role of a semi-permeable membrane in a PEM fuel cell. The performance of the radial flow fuel cell is dependent on the ionic concentration of the supporting electrolyte. The Ohmic resistance of the cell is a critical factor in the cell performance. The total

Ohmic resistance is a function of the individual resistive contributions of the electrodes, current collection leads, as well the electrolyte in the gap. Figure 3.1.4 shows that an increase of the sulfuric acid concentration from 0.5 M to 1 M significantly lowers the Ohmic resistance of the cell. For example, the cell exhibits similar potentials at 5000 μl min^{-1} at 0.5 M and 500 μl min^{-1} with 1 M sulfuric acid. Increasing the supporting electrolyte concentration increases electrical potential and maximum power at each flow rate.

Figure 3.1.7 presents a semi log plot of the fuel cell's Ohmic resistance as a function of the flow rate, at both 0.5 M and 1 M sulfuric acid concentrations. The resistance was calculated from the slope of the linear region of the polarization curves shown in Figure 3.1.4a. Note that the resistance values here also reflect those of the current collection wires and leads, which were measured as approximately 4 Ω using a digital multimeter.

This data shows that doubling the sulfuric acid concentration reduces the Ohmic resistance of the cell (in some cases by half) which results in higher achievable currents, lower potential losses, and higher fuel cell power. An increase in sulfuric acid concentration yields higher solution conductivity across the anode to cathode gap, thus reducing Ohmic losses. I expect a reduction in the Ohmic losses of nearly half when doubling the sulfuric acid concentration since the conductivity of the solution increases from 2 S cm^{-1} at 0.5 M to 4 S cm^{-1} at 1 M, measured using a conductivity meter. I expect the resistance to depend on the conductivity since the small gap between the anode and cathode provides an ionic bridge for the proton transfer. In the limit of small *g*, an approximation for

the gap's resistance is $R=g/\sigma\pi h(D_a+g)$, where σ is the local conductivity of the solution in the gap. Based on the equation above, resistance is inversely proportional with σ and h, and varies nearly linear with the gap width g. Although larger values of h reduce the gap's electrical resistance, the laminar flow becomes more susceptible to perturbations as discussed in section 3.1. Reducing the gap length should reduce the resistance and in this work is limited by manufacturing methods used and the ability to control the diffuse fuel and oxidant interface in the gap. I estimate the gap's electrical resistance to be approximately 3.3 Ω, based on the cell geometry and the solution conductivity of 1 M sulfuric acid.

Figure 3.1.7 also shows that increasing the flow rate reduces Ohmic resistance of the cell. For example, at 0.5 M, an increase in the flow rate by 14 times reduces the Ohmic resistance by a factor of 2.6. This data suggests that there is a limit to the reduction of Ohmic losses by an increase of the flow rate. At 1 M supporting electrolyte, the resistance drops rapidly over the first decade of increasing flow rate, but appears to asymptote at higher flow rates. As described in the next section, increasing the flow rate decreases the fuel utilization, and so flow rate can be used to tune the performance of the cell.

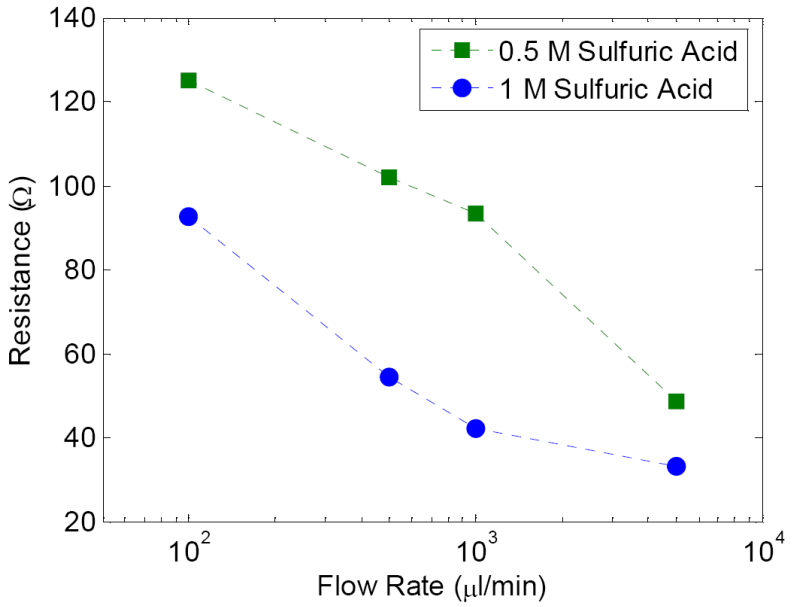

Figure 3.1.7: Calculated Ohmic resistance versus flow rate (ratio 1:1 fuel to oxidant). Supporting electrolyte concentrations are denoted in the legend. The Ohmic resistance is extracted from the linear region of the polarization curves shown in Figure 3.1.4.

Fuel utilization

The fuel cell potential and power increases with flow rate, but results in lower fuel utilization. Assuming complete fuel dissociation (as shown in equation (3.1.1)), the fuel utilization is expressed as

$$\eta_i = \frac{I_i}{nFCQ_i}, \tag{3.1.5}$$

where I is the measured current at a flow rate Q, n is the number of electrons transferred per mole (2 for formic acid), F is Faraday's constant, and C is the concentration of formic acid (0.04 M). Figure 3.1.8 shows a semi log plot of η

against the flow rate for 0.5 M and 1 M sulfuric acid concentration. The utilization is calculated using the maximum measured current in the cell. The fuel utilization decreases with increasing flow rate from a maximum value of 0.58 at 100 μl min^{-1} to a minimum value of 0.04 at 5000 μl min^{-1} for the 1 M sulfuric acid, and from 0.31 at 100 μl min^{-1} to 0.02 at 5000 μl min^{-1} for the 0.5 M sulfuric acid. I attribute the decrease in the fuel utilization to the decrease in residence time for the formic acid oxidation.

The radial flow fuel cell exhibits a fuel utilization of 58 % at a total power output of 4.1 mW and fuel flow rate of 100 μl min^{-1}. At the highest fuel flow rates of 5 ml min^{-1}, the fuel cell provided 12 mW at 4% fuel utilization (i.e. nearly factor of three increase in power at the expense of fuel utilization). Lower flow rates result in enhanced fuel utilization and higher energy density. Higher flow rates have greater power densities but lower utilization. It may be possible to increase the power at low flow rates without compromising utilization by increasing the concentration of the supporting electrolyte, increasing the surface area of the catalyst, or by using a fuel with greater electrochemical activity.

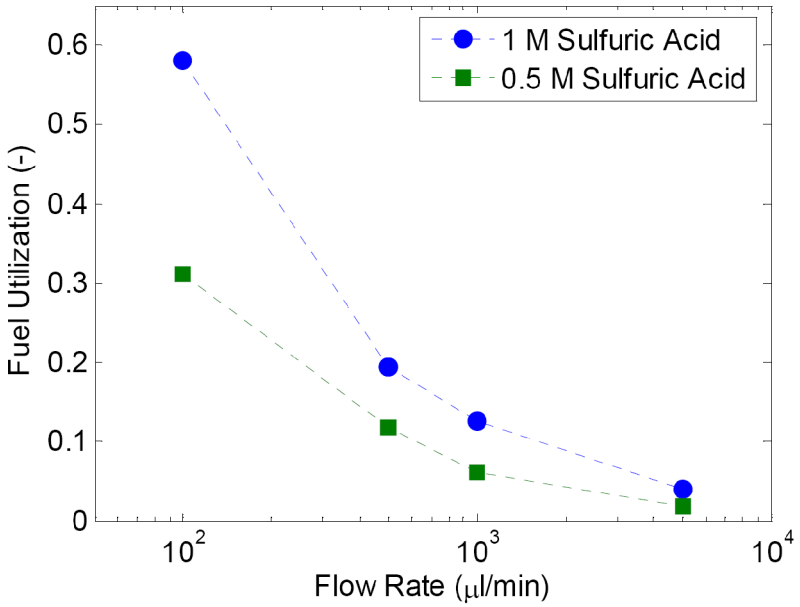

Figure 3.1.8: Sequential flow fuel utilization as a function of 1:1 fuel to oxidant flow rates. Fuel utilization is calculated using maximum current. Although lower flow rates utilize fuel more efficiently, maximum power is compromised.

3.1.5. Discussion

Parallel flow membraneless fuel cells mitigate some of the challenges associated with PEM fuel cells by using a diffuse interface that is not ion selective. The Peclet (*Pe*) number $Pe = UL/D$ defines the dominant transport processes in membraneless fuel cells, where U is the magnitude of the flow velocity, L is the characteristic length of diffusion, and D is the diffusion coefficient. At low Peclet numbers the dominant mode of transport is diffusive which mixes and depletes the reactants [33]. The diffusivity of formate, oxygen, and permanganate in an aqueous medium is approximately 1.5 $x10^{-5}$ cm^2 s^{-1}, 2.5 $x10^{-5}$ cm^2 s^{-1}, and 1.6 $x10^{-5}$ cm^2 s^{-1}, respectively [63]. Equivalent reactant

diffusivities imply that species transport by diffusion is not a very efficient mechanism to prevent anions such as permanganate from diffusing into the fuel stream or reaching the anode, causing reactant depletion and mixed potentials. Increasing the Peclet number (i.e. by increasing the flow rate) results in less diffusive mixing at the expense of fuel utilization. At higher Peclet numbers the mass transport boundary layer is thinner which enhances mass transport at the electrodes, but a greater fraction of the unreacted fuel is advected out of the cell and wasted.

Sequential flow fuel cells with porous electrocatalysts have distinct transport features. First, the porous electrodes have high surface area and narrow pores which reduce the length scales over which concentration gradients exist, reducing concentration polarization and improving fuel utilization. Second, the sequential flow pattern enables independent control of reactant flow rates and eliminates the linear diffuse interface responsible for reactant mixing and crossover. On the other hand, sequential flow results in mixing and crossover of fuel into the cathode if the fuel is not completely oxidized while passing through the anode. This requires careful tuning of the flow rates, electrocatalyst surface area, reactant concentrations, and current load. In addition, the radial design allows for independent variation of the projected electrode anode and cathode surface areas.

The sequential flow fuel cell exhibits polarization and power curves similar to both experimental and computational studies of parallel flow membraneless fuel cells. Our data reveals that increasing reactant flow rate

delays the onset of mass transport losses and extends the Ohmic regime resulting in higher peak power densities in agreement with previous studies [36, 41, 44, 66, 67]. Ohmic resistance also decreases with flow rate as was shown by Kjeang *et al.* The perceived decrease in Ohmic resistance in membraneless fuel cells may actually be a reduction in mass transport losses. Moreover, fuel utilization decreases with flow rate (or *Pe* numbers) as observed in parallel flow cells [33, 36] but the sequential cell attains higher fuel utilization than parallel flow designs because of the improved mass transport through the porous electrocatalysts. Figure 3.1.8 shows that the fuel utilization (η) is approximately twice as large for 1 M sulfuric acid as for 0.5 M and that η asymptotes at large flow rates for both cases. Utilization increases with ionic strength at low flow rates because the maximum current at low flow rates is dictated by the Ohmic resistance. The Ohmic resistance decreases with concentration which yields larger maximum current as shown in Figure 3.1.4. The utilization asymptotes at higher flow rates because in this regime the maximum current is controlled by mass transport.

Figure 3.1.9 presents a summary of the fuel cell performance. The peak power density is plotted against its respective current density, at each investigated electrolyte concentration and reactant flow rate. The slope of this plot is the voltage at which the peak power is observed which is approximately 0.55 V. Higher maximum power potentials are attractive for small scale fuel cells because DC voltage multiplication is more efficient at higher voltages and smaller numbers of cells in series are required to reach the desired voltage. The data also presents a correlation between the electrolyte concentration and flow rate. For

example, the power density at a flow rate of 100 µl min^{-1} and electrolyte concentration of 1 M is approximate to that of a flow rate of 1000 µl min^{-1} and electrolyte concentration of 0.5 M. This suggests that from an energy density standpoint, it is more attractive to have a higher electrolyte concentration because less volume and weight of reactants are required to produce the same power. Figure 3.1.9 can be used as a design curve for predicting fuel cell performance for specific power and current needs.

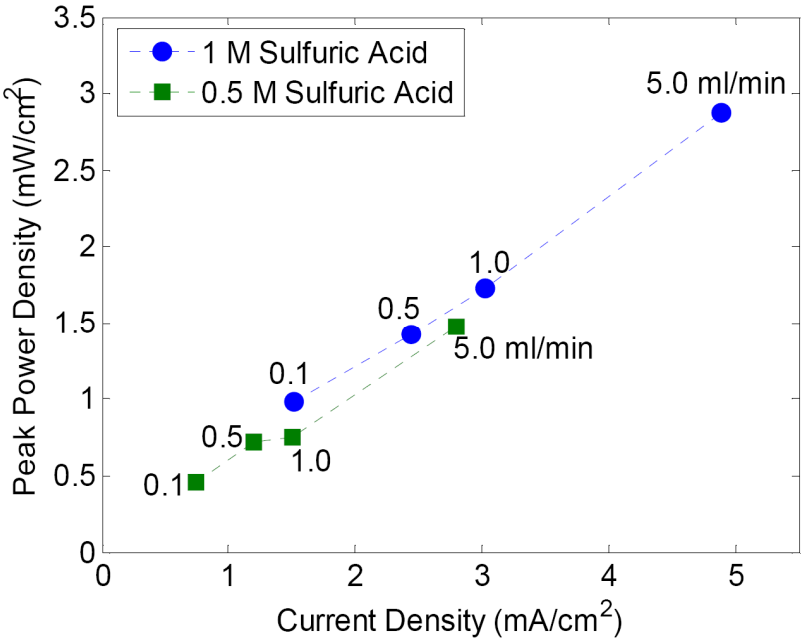

Figure 3.1.9: Sequential flow fuel cell peak power density as a function of current density, electrolyte concentration, and flow rate. The slope of the line (~0.55 V) is the operating voltage at peak power.

3.1.6. Conclusions

A novel convective flow membraneless microfluidic fuel cell with porous disk electrodes is described. In this fuel cell design, the fuel flows radially

outward through a thin disk shaped anode and across a gap to a ring shaped cathode. An oxidant is introduced into the gap between anode and cathode and advects radially outward to the cathode. This fuel cell differs from previous membraneless designs in that the fuel and the oxidant flow in series, rather than in parallel, enabling independent control over the fuel and oxidant flow rate and the electrode areas. The cell uses formic acid as a fuel and potassium permanganate as the oxidant, both contained in a sulfuric acid electrolyte. The flow velocity field is examined using microscale particle image velocimetry and shown to be nearly axisymmetric and steady. The results show that increasing the electrolyte concentration reduces the cell Ohmic resistance, resulting in larger maximum currents and peak power densities. Increasing the flow rate delays the onset of mass transport and reduces Ohmic losses resulting in larger maximum currents and peak power densities. An average open circuit potential of 1.2 V is obtained with maximum current and power densities of 5.35 mA cm^{-2} and 2.8 mW cm^{-2} respectively (cell electrode area of 4.3 cm^2). At a flow rate of 100 μL min^{-1} a fuel utilization of 58% is obtained.

3.2. Counter Flow Fuel Cell

3.2.1. Motivation

In the previous section, I presented a membraneless fuel cell where the fuel and oxidant flow in series. The sequential flow design realigns and shortens the linear diffuse interface responsible for reactant mixing and crossover in parallel flow schemes. I also used porous electrodes to increase the overall reaction surface area that results in higher fuel utilization. In this serial design any unutilized fuel will either mix and deplete the oxidant, or react at the cathode and cause mixed potentials. Therefore the sequential flow pattern requires complete utilization of the reactant traveling through both electrodes, or pairing a fuel and oxidant with selective catalysts. Kjeang et al. presented a parallel flow scheme where the reactants also flow through porous electrodes prior to their diffusive interface [38]. The flow through design alleviates complications with the diffusion boundary layer growth on sidewall electrodes, which is typical in parallel flow architectures. In both studies, power density increased with increasing flow rate, countered by a decrease in fuel utilization. Moreover, stronger electrolytes increase the power density due to enhanced conductivity in the fuel cell.

In this section, I present a counter flow membraneless microfluidic fuel cell where a non-reacting electrolyte separates the reacting streams. This architecture differs from previous works in literature and the sequential flow in that reactants do not directly interface. The separation diverts the reactants to different outlets, where in typical parallel flow configurations usually a single exit

port is dedicated for all the streams. The possible reuse of the reactants is further explored in Section 3.3; in this section I investigate the effects of the separating electrolyte on the fuel cell performance and the overall fuel utilization and power density behavior of this architecture.

Figure 3.2.1 shows a schematic of the counter flow pattern with porous electrodes. The fuel is introduced from port 1, undergoes oxidation at its porous anode, and then exits the cell through port 2. The oxidant, in a similar manner, is introduced from port 3, undergoes reduction at its porous cathode, and then exits through port 4. The electrolyte serves as a non-reacting, ion conductive medium that is introduced at the center of the cell through port 5. The electrolyte prevents the direct interface between the fuel and oxidant. The electrolyte flow splits equally to exit through ports 2 and 4. The electrons are conducted externally from the anode to cathode through a characterization platform (not shown). Figure 3.2.2 shows particle streak imaging of the counter flow scheme, with the electrolyte stream absent for simplifying the visualization.

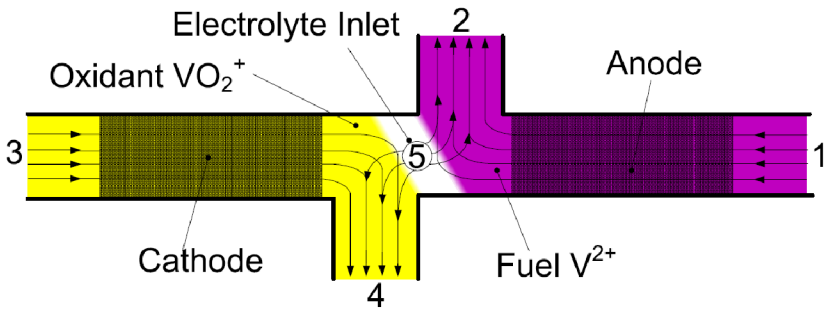

Figure 3.2.1: Counter flow fuel cell schematic. The reactants are introduced at opposite ends (1,3) and flow through porous electrodes. An electrolyte is introduced at the interface of the reactants (5) which direct their flow to outlets (2,4) while completing the electrochemical circuit.

The counter flow design provides several improvements to previous multi-stream designs. Sun et al. [41] presented a three stream membraneless fuel cell using the parallel flow scheme. While the design effectively separated the fuel and oxidant, the distance between the electrodes was increased - resulting in higher Ohmic losses - and a concentration boundary layer still developed over the sidewall electrodes, causing depletion zones for the reactants downstream. Jayashree et al. [44] and Brushett et al. [50, 51] also presented microfluidic fuel cells with flowing electrolytes, however the separation was maintained with a solid porous diffusion layer rather than fluidics, thereby enlarging the fuel cell and adding complexity to its fabrication and construction. The counter flow design I present here prevents the reactants from mixing in two ways: (i) by using hydrodynamics to prevent diffusive mixing at the interface, and (ii) by

independently collecting the reactants through separate outlets, allowing for a possible reuse.

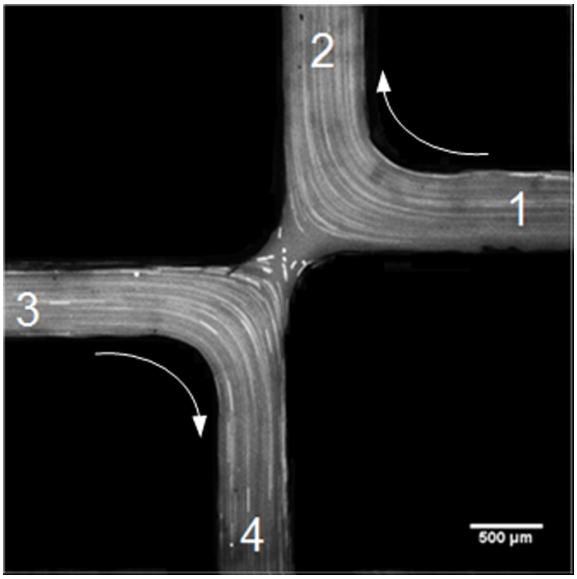

Figure 3.2.2: Particle streaking flow visualization of a counter flow scheme. One stream flows from inlet 1 to outlet 2, while the other stream flows from inlet 3 to outlet 4. For simplicity in the imaging, these two streams are interacting without the source of an electrolyte in the center.

3.2.2. Fuel cell construction

The fuel cell consists of three PMMA layers fabricated using a carbon dioxide laser ablation system (M360, Universal Laser Systems, Scottsdale, AZ). The bottom layer has holes cut out for inserting 0.127 mm sections of platinum wire (SPPL-010, Omega Engineering, Stamford, CT) that serve as current collectors. The wires come in contact with the electrodes which are 1 mm tall and 10 mm long stacked sheets of Toray carbon paper (E-TEK, Somerset, NJ) housed in the middle layer. The spacing between the electrodes is 1 mm. The active top

projected electrode area in the cell is 0.1 cm^2, and all absolute current and power numbers are normalized by this area. The top layer of the fuel cell seals the assembly with holes cut out for fluidic access. Liquids are delivered to the cell using 1.5 mm Tygon™ tubing (EW-06418-02, Cole Parmer, Vernon Hills, IL) bonded to the ports with quick dry epoxy. The three PMMA layers are adhered using double sided adhesive Mylar (3M, St. Paul, MN).

The electrolyte and both reactants are delivered to the fuel cell by two independent programmable syringe pumps (KDS200, KD Scientific, Holliston, MA). Reactant flow rates ranged from 50 to 2000 $\mu l\ min^{-1}$, and electrolyte flow rates ranged from 0 to 600 $\mu l\ min^{-1}$. The fuel cell leads are connected to a source meter (Model 2410, Keithley Instruments, Cleveland, OH) operating in galvanostatic mode. Galvanostatic measurements are taken in steps of 0.1 mA, starting from open circuit potential. The current and voltage are collected using a PC and Labview (National Instruments, Austin, TX) connected to the source meter via GPIB interface. After each change in the current, the cell requires 10 to 15 seconds to reach a steady state voltage. The voltages reported here are time averaged over 30 seconds after the transient response. Power and current density numbers reported here are normalized by the top projected electrode area of 0.1 cm^2.

For flow visualization, a similar cell to the one I electrochemically test is constructed. The cell's middle layer is ablated from 250 μm tall double sided adhesive Mylar, and no electrodes or separation electrolyte are present. The flow tracers are 10 μm fluorescent polystyrene microspheres (G1000, Duke Scientific,

Fremont, CA) diluted in DI water. The particle streaks are imaged using an epifluorescence microscope (AZ100, Nikon, Tokyo, Japan), 1X, 0.10 NA objective, and a cooled 16 Bit CCD camera (Cascade 512IIB, Roper Scientific, Tucson, AZ). The exposure time on the camera is set to 1 s and the flow rate of both streams is 5 μl min^{-1}.

3.2.3. Chemistry

Vanadium redox in acidic media served as our fuel and oxidant. Although vanadium has a lower energy density than methanol or formic acid, it has high activity on bare carbon, high open circuit potential, and can be regenerated [37]. I prepare 50 mM V^{2+} and VO_2^+ in 1 M sulfuric acid through electrolysis of VO^{2+}.

Reactants for the cell are obtained by first preparing 50 mM vanadium(IV) oxide sulfate hydrate (CAS 123334-20-3, Sigma Aldrich, St. Louis, MO) in sulfuric acid (CAS 7664-93-9, EMD Chemicals, Hibbstown, NJ) diluted to 1 M in 18.3 MΩ deionized water (Millipore, Billerica, MA). After mixing, a clear blue solution indicates the presence of the vanadium(IV) ion. An in-house electrolytic cell is fabricated using PMMA for the housing, Toray paper for the electrodes, and a Nafion membrane (NRE212, Fuel Cell Store, Boulder, CO) as the ion exchange medium [37]. The electrolytic cell generates the oxidation states vanadium(II) and vanadium(V) from the stock vanadium(IV) [63]. At the cathode (negative electrode) the reaction,

$$VO^{2+} + 2H^+ + e^- \leftrightarrow V^{3+} + H_2O \qquad E^o = 0.337\ \text{V vs. SHE}, \tag{3.2.1}$$

occurs, followed by

$$V^{3+} + e^- \leftrightarrow V^{2+} \qquad E^o = -0.255\ \text{V vs SHE}. \tag{3.2.2}$$

At the anodic (positive) half cell the reaction

$$VO^{2+} + H_2O \leftrightarrow VO_2^+ + 2H^+ + e^- \qquad E^o = 0.991\ \text{V vs SHE}, \tag{3.2.3}$$

occurs. To obtain V^{2+} as the fuel, the charge balance requires that the anodic half cell of the electrolysis setup be twice the volume of its cathodic counterpart. A nitrogen gas stream is constantly introduced to the cathodic half cell to maintain vanadium(II) stability [36]. After the fuel and the oxidant are prepared, they are extracted and used in the fuel cell at the anode and cathode as

$$V^{2+} \leftrightarrow V^{3+} + e^- \qquad E^o = -0.255\ \text{V vs SHE} \tag{3.2.4}$$

and

$$VO_2^+ + 2H^+ + e^- \leftrightarrow VO^{2+} + H_2O \qquad E^o = 0.991\ \text{V vs SHE}, \tag{3.2.5}$$

respectively. The separation electrolyte is sulfuric acid, diluted to 1 M or 2 M.

3.2.4. Results and Discussion

Fuel cell performance

Here I describe the variation of the fuel cell performance on the flow rate of the reactants, electrolyte, and the concentration of the separation electrolyte. Figure 3.2.3 presents polarization and power density curves for the counter flow fuel cell operating at 50 and 300 $\mu l\ min^{-1}$. In both cases, the reactant concentrations were 50 mM vanadium in 1 M sulfuric acid, and the separation electrolyte was 2 M sulfuric acid with a flow rate of 30 $\mu l\ min^{-1}$. The polarization data shows general fuel cell behavior present in both membraneless [55] and membrane based [3] designs. An initial drop in voltage is due to

activation losses at the electrocatalyst surface. The activation decay is followed by a linear region of potential drop due to Ohmic losses in the electrodes and ionic interface. At higher current densities (and low flow rates) a reaction boundary layer at the electrocatalyst surface prevents fresh vanadium from reacting, inducing a sharp drop in cell potential as observed for the 50 μl min^{-1} case at current densities in excess of 4 mA cm^{-2}.

Increasing the reactant flow rate should only reduce the mass transport associated losses in the cell potential. The potential losses (activation and Ohmic) are identical to a current density of less than 4 mA cm^{-2}. In excess of 4 mA cm^{-2}, the 50 μl min^{-1} case exhibits lower potentials than the 300 μl min^{-1} case, which I attribute to mass transport losses at the lower flow rate. I do not observe the drop in potential in the 300 μl min^{-1} case due to an extension of the Ohmic regime. Higher flow rates decrease the thickness of the reaction driven diffusion boundary layers thus enhancing the mass transport of the reactants to the catalyst sites [56].

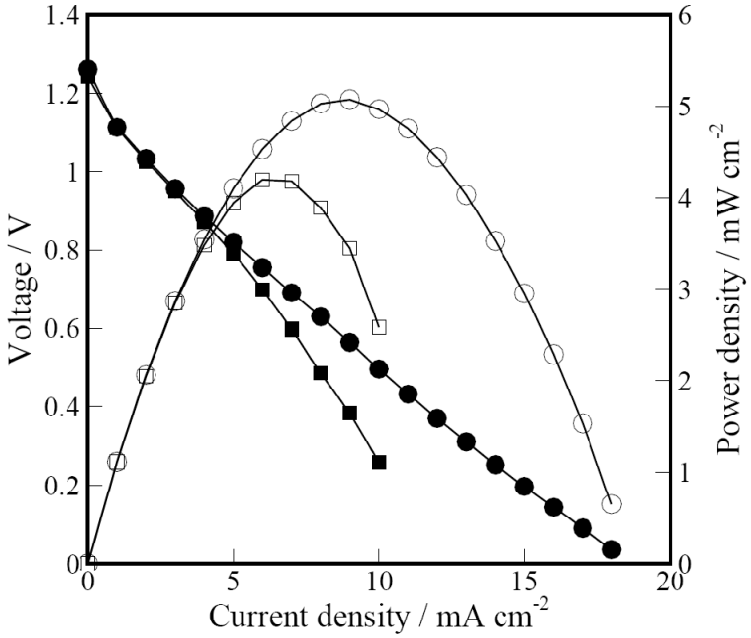

Figure 3.2.3: Polarization (filled symbols) and power density (open symbols) curves for the counter flow fuel cell operating at 50 µl min^{-1} (■) and 300 µl min^{-1} (●), and in both cases the separation electrolyte was at 30 µl min^{-1}. At higher flow rates, reaction and diffusion boundary layers at the electrode surface are thinner, which enhances reactant transport and yields higher currents.

The counter flow fuel cell features a separation electrolyte that helps maintain physical separation between the fuel and oxidant, while providing a highly conductive ionic interface to complete the electrochemical circuit. Figure 3.2.4 shows the effect of altering the electrolyte flow rate on the fuel cell polarization. The polarization curves show that potential and current density increase by approximately 0.1 V and 3 mA cm^{-2} when the electrolyte flow rate varies from 0 to 600 µl min^{-1}. In a membraneless fuel cell, the electrolyte

provides an electrochemical bridge from the anode to the cathode similar to the role of a semi-permeable membrane in a PEM fuel cell. I expect the resistance to depend on the gap conductivity and geometry. An approximation for the gap's resistance is $R=g/\sigma A$, where g is the gap length between the electrodes, σ is the local conductivity of the solution in the gap, and A is the cross sectional area of the gap. The separation electrolyte contains a higher concentration of sulfuric acid than the reactant streams and, at higher flow rates, occupies a larger zone in the gap between the electrodes which increases the effective conductivity of the solution. Therefore, the increase in potential is attributed to the reduction in Ohmic losses in the gap. The increase in cell performace is relatively small because the Ohmic losses are largely controlled by the distance between the electrodes, g, which is kept constant throughout our experiments. These results suggest that the minimum electrolyte flow rate may be used to maintain an effective reactant separation.

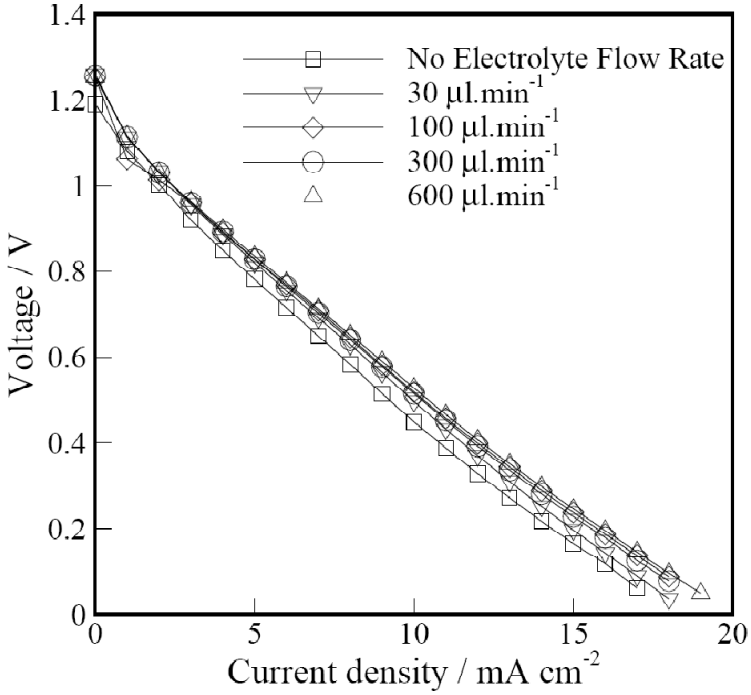

Figure 3.2.4: Fuel cell polarization curves for electrolyte flow rates ranging from 0 to 600 µl min^{-1}. The vanadium reactant concentrations are 50 mM supported in 1 M sulfuric acid flowing at 300 µl min^{-1}. The seperating electrolyte is 2 M sulfuric acid. As the separating electrolyte flow rate increases a marginal increase in overall current density and potential is observed.

Fuel utilization and power density

I have shown that increasing the reactant flow rate increases the fuel cell potential and power. However, the increase in power is at the cost of fuel utilization, described as

$$\eta = \frac{I}{nFCQ}, \tag{3.2.6}$$

where I is the measured current at a flow rate Q, n is the number of electrons transferred per mole (1 for vanadium redox), F is Faraday's constant, and C is the concentration of vanadium used (0.05 M). Using equation (3.2.6) and polarization data from Figure 3.2.3, the maximum fuel utilization at 50 and 300 µl min^{-1} are 24.9 and 8.3 %, respectively.

Figure 3.2.5 plots power density and fuel utilization as a function of reactant flow rate. The separation electrolyte was fixed at 30 µl min^{-1} and 2 M, and the sourced current density is 5 mA cm^{-2}. At this current density, the voltage increases from 0.8 V to 1.0 V across the flow rate range. As with previous findings [36, 38, 39], the fuel utilization drops drastically over the flow rate range, while the power increase is not as significant. In our case, a 20% increase in power over the tested flow rates is countered by a 91% drop in fuel utilization.

Equation (3.2.6) suggests that increasing the fuel utilization is best achieved by flowing low concentration reactants at low flow rates. The reaction residence times, reaction product advection, and transport due to diffusion at the reactant/electrolyte interface are all dependent on the flow rates of the reactants and electrolyte. However, it is also advantageous to expose the reactants to the largest possible electrocatalyst surface. Larger surface areas increase the reaction sites and reduce overall concentration boundary layers, resulting in an increase in extracted current. While the fuel cell can be designed to house larger electrode areas, the counter flow scheme I present allows the reactants to be recycled as they have not mixed.

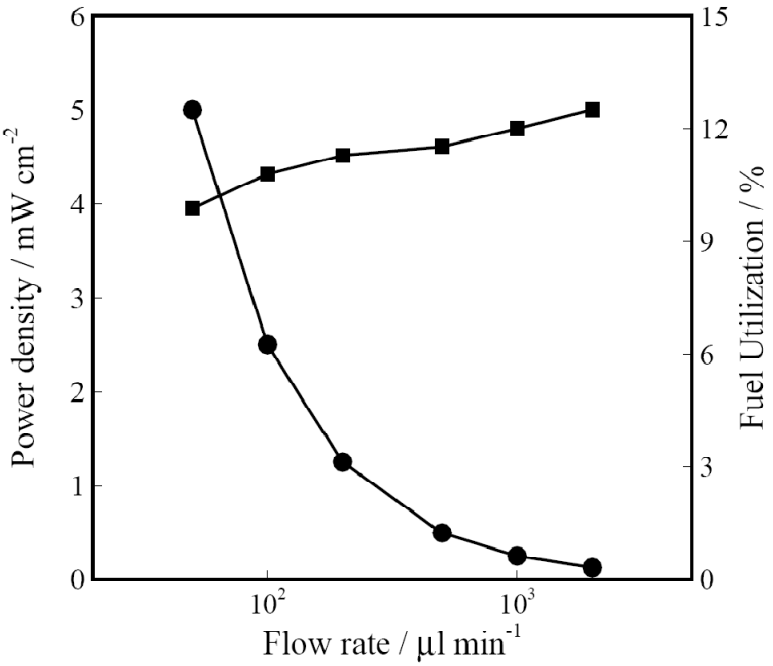

Figure 3.2.5: Power density (■) and fuel utilization (●) as a function of the reactant flow rate, under 5 mA cm^{-2} current density load. The separating electrolyte was fixed at 30 µl min^{-1} and 2 M. There is a drastic decrease in fuel utilization and moderate increase in power density.

3.2.5. Conclusions

A counter flow membraneless microfluidic fuel cell is presented, where a non-reacting electrolyte separates the reacting streams. In this fuel cell design, vanadium reactants flow through porous carbon electrocatalysts. A sulfuric acid stream is introduced in the gap between the electrodes and diverts the reactants to opposite and independent outlets. This fuel cell differs from other membraneless designs in its ability to maintain a constant separation between the reactants

without diffusive mixing. The fuel cell architecture allows electrolyte flow rates as low as $30\ \mu l\ min^{-1}$ to separate reactants. The reactants remain separated throughout their residence time in the fuel cell, do not mix diffusively, and are collected separately. Increasing the reactant flow rate results in an increase in potential and power density output. However, the increase in power output at higher flow rates results in a drastic loss in fuel utilization.

3.3. Multi-pass Fuel Cell

3.3.1. Motivation

Both of the sequential and counter flow designs featured (i) porous electrocatalysts that maximize reaction surface area and alleviate deficiencies with mass boundary layer depletion zones common in flat plate electrode designs, and (ii) a concise ionic interface where advection occurs in the direction of concentration gradients which mitigates diffusion of reactants. The shortened ion exchange zone comes at the cost of increased Ohmic resistance. One of the consequences of the designs that eliminate diffusive mixing is that the reactants (with or without a non-reacting electrolyte) do not interface over large areas which increases Ohmic losses. The radial flow fuel cell leverages the aforementioned design aspect by increasing the interfacial area in the azimuthal direction. This expansion retains the desirable concise ionic interface which reduces diffusive mixing, yet maintains a large interfacial surface area, which reduces Ohmic losses, by radial integration of the interface. The radial fuel cell has the challenge that requires special attention to the fuel, oxidant, and catalyst selection as one of the reactant streams is introduced to its counter electrode. The counter flow design, through the use of a separation electrolyte, maintains separation of the two reactants after their reaction and interface. The advantage of this design is that the unused reactants can be used again in a downstream reaction zone. In this way, the fuel utilization becomes decoupled from the flow rate which may ultimately yield higher overall power density and thermodynamic efficiency. However, the counter flow design exhibits higher Ohmic losses

because of the small interfacial area between the reactants. While a radial expansion of the counter flow scheme to increase the interfacial area is possible, it introduces complications with maintaining the flow pattern, as the total number of inlets and outlets increases significantly.

In this work, I present a membraneless microfluidic fuel cell that, for the first time, enables stacking of reaction zones analogous to membrane based fuel cell stacks. This design keeps the reactants separate and enables the reactants to be reused, increasing the fuel utilization of the cell and effectively decoupling the power density from the fuel utilization. The cell presented here integrates two reactant and electrolyte interfaces on a single fluidic chip allowing for multiple passes of the reactants. Figure 3.3.1 shows the flow pattern in the multi-pass microfluidic fuel cell. The shortened ion exchange zone reduces reactant mixing and the non reacting electrolyte ensures their separation. The reactants are reused at a downstream reaction zone, effectively increasing the overall interfacial area. In this manner the fuel utilization is decoupled from the flow rate which will ultimately yield higher overall power density and thermodynamic efficiency. In this flow configuration, the fuel and the oxidant are first introduced through a porous electrocatalyst. At the interface junction between the anode and the cathode, an electrolyte splits equally to direct the fuel and oxidant through independent channels leading from cell 1 into cell 2. The exact flow pattern is repeated in cell 2, and terminates with the fuel and oxidant flowing to independent outlets. Each interface is treated as an individual electrochemical cell with its own porous anode and cathode, and external contact for current sourcing.

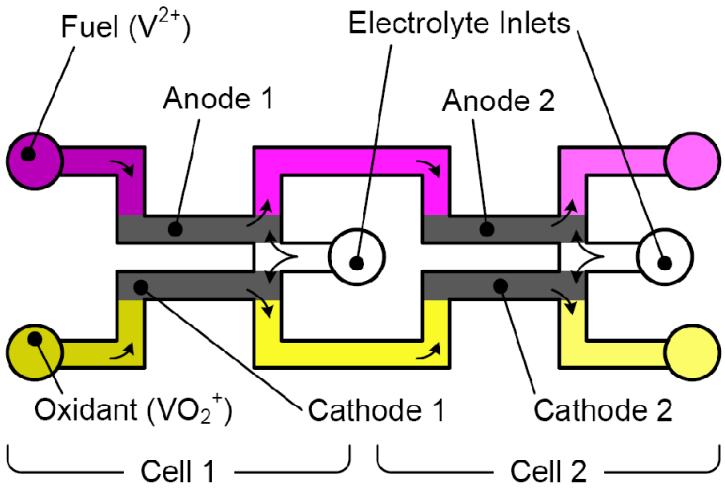

Figure 3.3.1: Top view schematic of the multi-pass fuel cell. After reacting through the porous electrodes in cell 1, the fuel and the oxidant are redirected by an electrolyte to cell 2. Arrows represent flow direction.

The multi-pass design (i) separates the reactants throughout the device, (ii) provides a high conductivity ionic exchange zone that reduces reactant diffusive mixing, and (iii) uses porous electrocatalysts to increase available reaction surface area. This design results in an effective increase in the ionic exchange cross sectional area by repeating interfaces, similar to a stacked PEM fuel cell architecture, exhibiting reduced reactant mixing compared to a single extended diffusive interface. It is difficult to maintain the stability of an extended interface due to an increase in downstream diffusive mixing and susceptibility to perturbations in elongated channels. Figure 3.3.2 shows flow visualization optical micrographs of the fuel cell design cell under various ratios of the flow rate of the reactants to that of the separating electrolyte. It is preferential to use lower

separating electrolyte flow rates as to not overwhelmingly dilute the reactants at each subsequent interface, and to increase the overall gravimetric power density and reduce pumping power associated with carrying a non-reacting electrolyte. The Reynolds number at each micrograph in Figure 3.3.2 is defined as $Re = UD_h\upsilon^{-1}$, where U is the average fluid velocity in the channel, D_h is the hydraulic diameter of the channel, and υ is the kinematic viscosity of the fluid. The purpose of the visualization is to investigate the onset of reactant mixing due to decreased separating electrolyte flow rate. Figure 3.3.2D suggests that even at electrolyte flow rates of only 6% the reactant flow rates, separation between the two streams is complete and little reactant crossover occurs. I have previously demonstrated that various separating electrolyte flow rates achieve similar fuel cell polarization, and concluded that the minimal electrolyte flow rate be used to separate reactants [59].

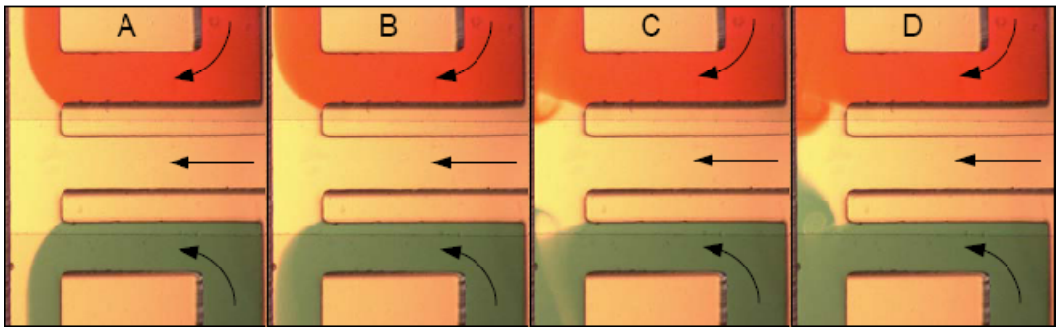

Figure 3.3.2: Optical micrographs showing reactant separation under various Reynolds (*Re*) number ratio of the reactants (colored) to that of the electrolyte (clear). (A) 1:1, (B) 4:1, (C) 10:1, and (D) 16:1, where a ratio unit corresponds to $Re = 6$. The Reynolds number is defined as $Re = UD_h/\upsilon$. Arrows represent the flow direction, and the channel width is 800 μm. The reactants remain separated even at large *Re* ratios.

3.3.2. Experimental methods

Fuel cell construction and characterization

The fuel cell consists of three PMMA layers fabricated using a carbon dioxide laser ablation system (M360, Universal Laser Systems, Scottsdale, AZ). The bottom layer has holes cut out for inserting 0.127 mm sections of platinum wire (SPPL-010, Omega Engineering, Stamford, CT) that serve as current collectors. The wires come in contact with the electrodes which are 1 mm tall and 8 mm long stacked sheets of Toray carbon paper (E-TEK, Somerset, NJ) housed in the middle layer. The distance between the parallel carbon anode and cathode electrodes is 1 mm. The active projected electrode area in the cell is 0.08 cm^2, and all absolute current and power numbers are normalized by this area. The top

layer of the fuel cell seals the assembly with holes cut out for fluidic access. Liquids are delivered to the cell using 1.5 mm tubing (Tygon™ EW-06418-02, Cole Parmer, Vernon Hills, IL) bonded to the ports with quick dry epoxy. The three PMMA layers are adhered using double sided adhesive Mylar (3M, St. Paul, MN).

The electrolyte and both reactants are delivered to the fuel cell by two independent programmable syringe pumps (KDS200, KD Scientific, Holliston, MA). Reactant flow rates ranged from 50 to 500 μl min^{-1}, and electrolyte flow rates ranged from 0 to 250 μl min^{-1}. I record polarization data for cell 1 and cell 2 using a source meter (Model 2410, Keithley Instruments, Cleveland, OH) and a potentiostat (VersaSTAT 4, Princeton Applied Research, Oak Ridge, TN) respectively. I hold cell 1 at a fixed current density, and then completely polarize cell 2 by galvanostatic steps. I report the average cell 2 voltage after it equilibrates for 10-15 seconds. I then step the cell 1 current density, and repeat the polarization for cell 2.

Chemistry

I use vanadium redox species in acidic media (V^{2+}/V^{3+} at the anode and VO_2^+/VO^{2+} at the cathode) to characterize the fuel cell. While vanadium as a fuel exhibits lower energy densities than alcohols or organic acids, its high activity on bare carbon and its high open circuit potential make it an appealing selection for testing new microfluidic fuel cell architectures. I prepare 50 mM V^{2+} and VO_2^+ in 1 M sulfuric acid through electrolysis of VO^{2+}.

Reactants for the cell are obtained by first preparing 50 mM vanadium(IV) oxide sulfate hydrate (CAS 123334-20-3, Sigma Aldrich, St. Louis, MO) in sulfuric acid (CAS 7664-93-9, EMD Chemicals, Hibbstown, NJ) diluted to 1 M in 18.3 MΩ deionized water (Millipore, Billerica, MA). After mixing, a clear blue solution indicates the presence of the vanadium(IV) ion. An in-house electrolytic cell was fabricated using PMMA for the housing, Toray paper for the electrodes, and a Nafion membrane (NRE212, Fuel Cell Store, Boulder, CO) as the ion exchange medium [37]. The electrolytic cell generates the oxidation states vanadium(II) and vanadium(V) from the stock vanadium(IV) [63]. At the cathode of the electrolytic cell the reaction

$$VO^{2+} + 2H^{+} + e^{-} \leftrightarrow V^{3+} + H_2O \qquad E^{o} = 0.337\ \text{V vs. SHE} \tag{3.3.1}$$

occurs, followed by

$$V^{3+} + e^{-} \leftrightarrow V^{2+} \qquad E^{o} = -0.255\ \text{V vs SHE}\ . \tag{3.3.2}$$

At the anodic half cell the reaction

$$VO^{2+} + H_2O \leftrightarrow VO_2^{+} + 2H^{+} + e^{-} \qquad E^{o} = 0.991\ \text{V vs SHE} \tag{3.3.3}$$

occurs. To obtain V^{2+} as the fuel, the charge balance requires that the anodic half cell of the electrolysis setup be twice the volume of its cathodic counterpart. A nitrogen gas stream is constantly introduced to the cathodic half cell to maintain vanadium(II) stability [36].

At the fuel cell anode the oxidation reaction

$$V^{2+} \leftrightarrow V^{3+} + e^{-} \qquad E^{o} = -0.255\ \text{V vs SHE} \tag{3.3.4}$$

occurs and at the cathode the reduction

$$VO_2^+ + 2H^+ + e^- \leftrightarrow VO^{2+} + H_2O \qquad E^o = 0.991\,V \text{ vs SHE} \tag{3.3.5}$$

occurs [63].

3.3.3. Results and discussion

In this section I present polarization results for two cells stacked fluidically in series and electrically in parallel and compare it to the performance of a single cell. I also present the effects of reactant and separating electrolyte flow rate on the polarization of each fuel cell in the device, and investigate how the polarization of cell 1 affects that of cell 2. I conclude with a discussion on fuel utilization and overall efficiency of stacked microfluidic fuel cells.

Stack polarization

The multi-pass fuel cell allows for on-chip reactant recycling and can be analyzed as a single microfluidic fuel cell. It is similar to a PEM stack with bipolar plates in that the reactants pass serially through several reactive zones. I electrically connect cell 1 and cell 2 in parallel, i.e. a common anode and common cathode. When the reactants are subjected to two ion exchange zones the effective cross sectional area of the fuel cell doubles. This area increase results in an effective reduction in overall Ohmic losses since the fuel cell resistance can be approximated as $R=g/\sigma A$, where g is the length between the electrodes, σ is the conductivity of the solution in the gap, and A is the cross sectional area of the ion exchange zone. Figure 3.3.3 compares polarization and power density curves between a single and the multi-pass microfluidic fuel cells electrically connected in parallel. In this case the reactant and the separating electrolyte flow rates are 500 and 25 $\mu l\,min^{-1}$, respectively. The Ohmic loss differences are distinct

between the two cases, where the slope of the linear region of the stacked cell is approximately half that of the single cell. I do not readily observe any curvature in the polarization curves that would typically be associated with activation or mass transport losses. Vanadium redox species exhibit fast electrode kinetics on bare carbon, and at 500 μl min^{-1} mass transport losses are delayed and the majority of the polarization curve reflects the Ohmic losses.

The peak power density (and its respective current density) increases from 7.5 to 16 mW cm^{-2} upon doubling the number of fuel cell passes. The maximum fuel utilization also increases from 6 to 11%, calculated as

$$\eta = \frac{i \cdot A}{nFCQ}, \tag{3.3.6}$$

where i is the maximum measured current density, A is the top projected electrode area, n is the number of electrons transferred, F is Faraday's constant, C is the concentration of the fuel, and Q is the fuel flow rate. This design presents the first example of a membraneless microfluidic fuel cell that reuses reactants, in contrast to multichannel systems that employ common manifolds for inlets and outlets, as shown by Hollinger et al [68].

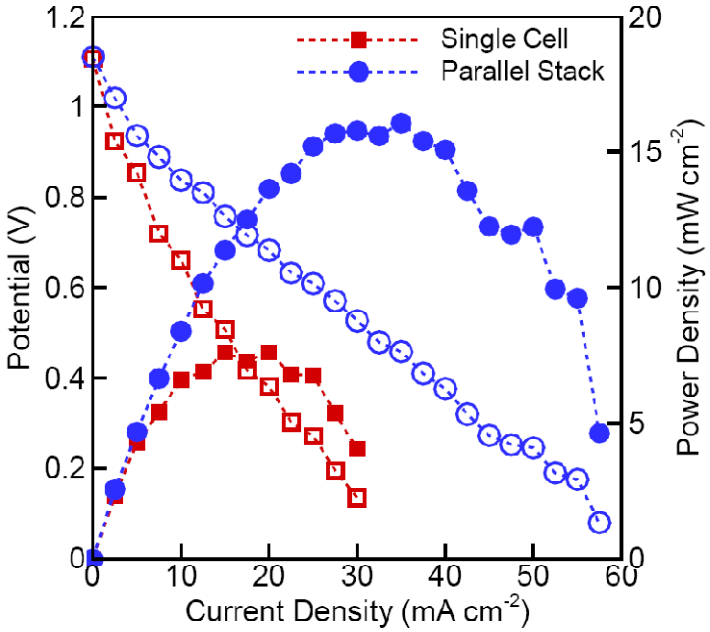

Figure 3.3.3: Polarization and power density curves for single and stacked cell (common anodes, common cathodes) configurations. By doubling the number of interface zones, both the maximum power density and maximum fuel utilization nearly double.

The vanadium fuel utilization values reported here are lower than large scale, membrane based [69] and microfluidic membraneless [38] fuel cells, which report utilization values larger than 90%. In this work I are characterizing our architecture using low vanadium concentrations and higher flow rates. Both of these parameters result in decreased reaction rates at the electrode surface, and thus lower fuel utilization. While the fuel concentration and flow rate can be tuned to achieve near complete utilization, the focus of this study is to enable

higher power density from larger flow rates and increased fuel utilization from reactant reuse.

Individual fuel cell polarization

While the primary interest is the power output of the overall stack, it is important to understand how the polarization of one cell in the stack influences that of downstream cells [70, 71]. Figures 3.3.4A, B, and C show polarization data for cell 1 and cell 2 at reactant/electrolyte flow rate ratios of 50/25, 500/250, and 500/25 (in $\mu l\ min^{-1}$), respectively. Cell 2 is downstream of cell 1 and its potential is dependent on the local reactant concentration and flow conditions which are modified by the operation of cell 1; therefore cell 2's polarization is noted as a function of the current density of cell 1 in each figure. Here I detail the effects of reactant and electrolyte flow rate on the potential output of the individual fuel cells.

In all three flow rate cases, I observe lower maximum current densities from cell 2 as I increase the current density from cell 1. For example, in Figure 3.3.4B, cell 2's maximum current density drops from 22.5 mA cm^{-2} to 12.5 mA cm^{-2} when I increase cell 1's current density from zero (open circuit potential) to 20 mA cm^{-2}. I attribute this decrease in cell 2's current density to lower reactant concentrations onset by dilution and utilization from cell 1. Lower reactant concentrations in the fuel cell result in current density losses due to lower reaction rates [72], and Nernstian potential losses due to a decrease in species activity and net Gibbs free energy [3].

The decrease in cell 2's maximum current density due to cell 1 is accentuated at low flow rates. For example, Figure 3.3.4A shows that at the 50 μl min^{-1} reactant flow rate, cell 2's highest current density is approximately 25% of cell 1's current. At high reactant (500 μl min^{-1}) and low electrolyte (25 μl min^{-1}) flow rates shown in Figure 3.3.4C, I observe nearly equivalent maximum current densities from both cell 1 and cell 2 over the entire range of cell 1's current density. At low reactant flow rates, cell 1 uses a larger fraction of the available reactants and results in lower reactant concentrations exiting cell 1. This effect results in a drastic decrease in cell 2's current density with larger cell 1 current densities.

I also consider the effect of the separating electrolyte flow rate on the individual cell polarization. Figures 3.3.4B and 3.3.4C show very similar polarization curves for cell 1 at the flow rate cases 500/250 and 500/25. Since the reactions occur prior to the three stream interface, the first cell's operation is not dependent on the separating electrolyte flow rate, consistent with our previous findings [59]. However, polarization curves with varying separating electrolyte flow rates are not equivalent in cell 2. At larger separating electrolyte flow rates, I observe a decrease in cell 2's current density with increasing cell 1 current density. For example, comparing figures 4B and 4C I see that cell 2's current density decreases by 5 mA cm^{-2} (at cell 2=0.4 V and cell 1 at maximum current density) when higher electrolyte flow rates are used. As the separating electrolyte flow rate increases I expect (i) enhanced mass transport at cell 2's electrode surfaces which results in higher current densities and (ii) decreased reactant

availability in cell 2 due to dilution from the added electrolyte which reduces reaction rates and results in lower current densities. From the polarization curves in Figures 3.3.4B and 3.3.4C it is apparent that larger electrolyte flow rates are detrimental to the performance of downstream cells. Under these conditions, the losses due to reactant dilution dominate enhancements of mass transport.

In parallel flow membraneless designs, species mixing by diffusion induces potential losses due to reactant crossover and depletion. In the current architecture the concentration gradients at the interface are aligned with the bulk fluid flow. At each reaction zone reactant diffusion is dependent on the local Peclet (*Pe*) number, where $Pe=(\nu/D)\times Re$, and (ν/D) is the Schmidt number (ratio of kinematic viscosity to diffusivity), and *Re* is the Reynolds number. In dilute aqueous solutions, I estimate the Peclet number as $Pe=1000\times Re$, and thus our smallest *Pe* number would approximately equal 6000. I can therefore deduce that cross species diffusion in the reaction zone is small.

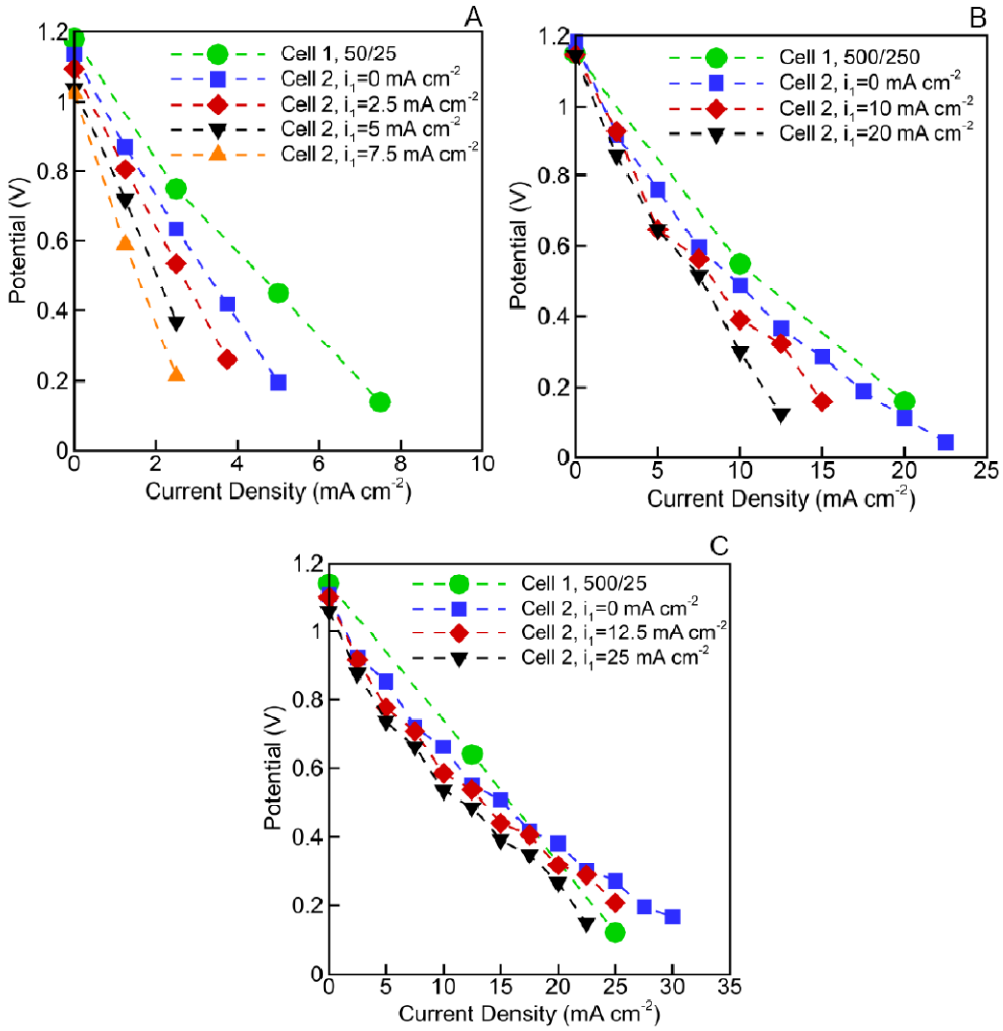

Figure 3.3.4: Polarization curves at (A) 50 µl min^{-1} reactant and 25 µl min^{-1} separating electrolyte flow rate, (B) 500 µl min^{-1} reactant and 250 µl min^{-1} separating electrolyte flow rate, and (C) 500 µl min^{-1} reactant and 25 µl min^{-1} separating electrolyte flow rate. The current density i_1 denoted in the legend reflects the galvanostatic state of cell 1 during cell 2's polarization. In all three cases higher current densities from cell 1 decreases the maximum current density of cell 2.

Fuel utilization

I calculate the overall fuel utilization from a two cell system as

$$\eta_o = \left(\frac{i_1}{nFCQ} + \frac{i_2}{nFCQ} \right) \cdot A, \tag{3.3.7}$$

Figure 3.3.5 plots the fuel utilization from cell 1 alone as well as the overall fuel utilization using equation (3.3.7) for the flow rate cases of 50/25 and 500/25. The fuel utilization is plotted as a function of the cell 1 current density and the maximum current from cell 2. I observe that fuel utilization increases linearly with increasing cell 1 current density, consistent with equation (3.3.7). I also note that the fuel utilization decreases with increasing flow rate, consistent with previous observations [59, 68, 73]. The maximum fuel utilization from cell 2 - when cell 1 current density is zero (i.e. no fuel is used in cell 1) - is approximately equal to the maximum fuel utilization from cell 1, regardless of the flow rate. This result shows that both cells operate nearly identical if treated individually. The near doubling of power density (Figure 3.3.3) and fuel utilization (solid over open symbols) shown in Figure 3.3.5 is due to equal contributions from both cells. Figure 3.3.5 shows that the fuel utilization for two cells is twice as large as a single cell when high flow rates (500/25) are used. When the lower flow rates are used (50/25), the fuel utilization is larger for two cells than for a single cell. For example, at low flow rates (50/25), the combined fuel utilization at 2.5 mA cm^{-2} is 3.2 higher than the single cell. In contrast, at higher flow rates (500/25) the fuel utilization for the combined cells is approximately twice that of the single cell across all current densities. If I operate

at low current densities, higher flow rates reduce the polarization influence from one cell to the next. Figure 3.3.5 suggests that I can increase fuel utilization by increasing the number of passes at high flow rates. In this configuration I can achieve both high fuel utilization and power output from the fuel cell.

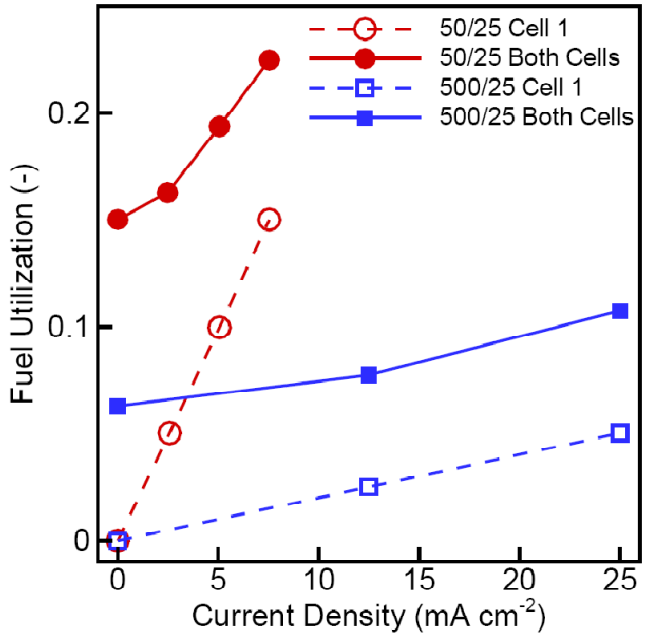

Figure 3.3.5: Comparison of overall fuel utilization for cell 1 (open symbols) and both cells (filled symbols) for 50 µl min^{-1} (●) and 500 µl min^{-1} (■) reactant flow rate. The separating electrolyte flow rate is 25 µl min^{-1}. The increase in fuel utilization is an advantage of recycling the reactants.

3.3.4. Conclusions

The performance of parallel flow based laminar flow fuel cells are limited by mass transport boundary layer growth over flat plate electrodes and diffusive broadening at the interface of fuel and oxidant. High flow rates are used in an

effort to diminish these challenges but result in wasted reactants that advect out of the system before completely reacting. In this work, I use porous electrocatalysts to maximize reaction surface area and brief ionic interface zones where reactant diffusion and mixing are mitigated. The multi-pass fuel cell design successfully recycles reactants from one cell to the other through the use of multiple interfaces, which increases both the overall fuel cell power and efficiency of the fuel cell. This work represents the first example of reusing reactants using stacked microfluidic fuel cell architectures, analogous to membrane based stacked fuel cell systems. The influence of one interface on the next is prominent at low reactant flow rates and high current densities. The power of cell 2 decreases with decreasing reactant flow rate, increasing electrolyte flow rate, and increasing upstream cell current density. When the two interfaces are interconnected to form a single cell, I observe that peak power density and fuel utilization is doubled relative to single cell. This design allows independent and uncoupled control over desired potentials and current densities through prescribing a specific number of interfaces.

CHAPTER 4

The Role of Geometry on Microfluidic Fuel Cell Metrics

4.1. Motivation

In the previous chapter, I presented three novel microfluidic flow fields that alleviate complications with reactant mixing and boundary layer limitations, which are typically intrinsic in parallel flow architectures. To date, however, the majority of the experimental work in membraneless microfluidic fuel cells is aimed at presenting new designs and demonstrating proof of concept. Systematic characterization of these devices, including those presented in Chapter 3, has been limited to the flow rate and chemistry of the reactants. While proper tuning of the chemistry and flow conditions optimize the operation of the fuel cell, optimizing the geometry as well will further improve the power output.

Various computational efforts that investigate the effects of the channel's and electrode's geometry are available. Park et al. modeled and studied the effect of the electrode spacing and the reactant interface profile on fuel utilization, and found that reducing the interfacial area between the reactant streams reduces crossover but also limits utilization [74]. Sprague et al. and Ebrahimi Khabbazi et al. modeled the effects of reactant crossover on microfluidic fuel cell polarization at various electrode lengths and electrode spacing, and reported that while reducing the electrode spacing mitigates the Ohmic losses, it also sets a greater possibility of reactant crossover and mixed potentials, especially at increased electrode lengths [75, 76]. On the other hand, experimental work on characterizing the effects of geometry on the performance of microfluidic fuel

cells is limited. Liu et al. showed that the power density of a micro borohydride fuel cell increases when the spacing between the anode and the cathode is reduced from 4 cm to 2 cm [77]. Jayashree et al. discussed a similar effect in a parallel stream laminar flow fuel, where the power output from the fuel cell increased by reducing the channel width from 2 cm to 0.05 cm [73].

In this chapter, I present an experimental setup to vary and characterize the effects of the microfluidic and electrode geometry on the polarization of a single reactant membraneless fuel cell, as shown in Figure 4.4.1. I make use of a single reactant because it removes complications that may arise from a dual or tri-stream interface, such as flow perturbations that might cause reactant crossover and mixed potentials. A single reactant fuel cell leverages differences in the Gibbs free energy of one species at two different electrode surfaces. Such reactions occur repeatedly through enzymatic and microbial means in biological systems, but may also occur in inorganic systems when the electrochemical activity of a molecule differs on two different surfaces. A prime example is the reduction-oxidation (redox) of hydrogen peroxide on platinum and gold surfaces, which respectively act as anode and cathode when present in the same electrochemical cell. The inspiration for using hydrogen peroxide comes from extensive research done on bimetallic catalytic nanomotors, which rely on the abovementioned differences in surface activity to propel themselves in a single reactant (fuel) medium [78-81].

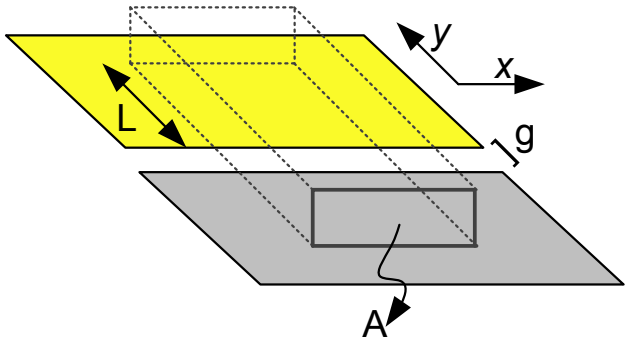

Figure 4.1.1: Schematic showing the geometric features of the single reactant membraneless microfluidic fuel cell. L is the electrode length (equal for both electrodes), A is the interfacial area between the two half-cells, and g is the electrode spacing on the substrate. The flow direction is either in the x or y direction as shown.

I also implement flat plate electrodes for the electrochemical characterization of the fuel cell. Porous electrodes improve mass transport by increasing the Sherwood number, $Sh = kL_c/D$, where k is the heterogeneous mass transport coefficient, L_c is the characteristic length of the diffusion layer, and D is the diffusion coefficient. Figure 4.1.2 compares the Sherwood number at low Reynolds numbers for a 78% porous bed [58] and flat plate [82] electrodes. Both electrode structures benefit from increased flow rate since the mass transport coefficient increases. Using flat plate electrodes ensures a controlled and comparable cell to cell characterization in terms of electrode length and surface area. Porous structures, despite their aforementioned advantages, may have random pore distributions that would alter mass transport and electrocatalyst

loading. Since the goal is to characterize, and not optimize, the fuel cell's power density and fuel utilization, I will forego the use of porous electrodes in this study.

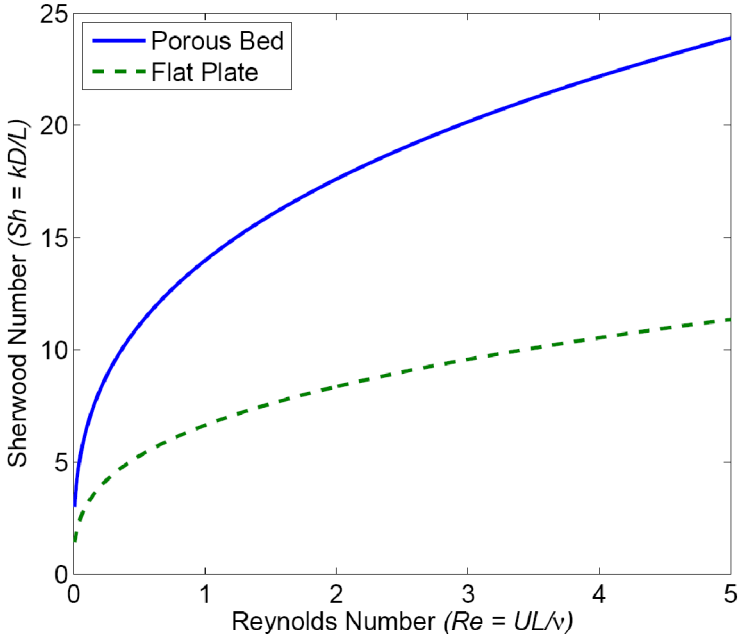

Figure 4.1.2: Laminar flow Sherwood number scaling with increasing Reynolds number for porous beds (solid line) and flat plates (dashed line).

4.2. Experimental setup

4.2.1. Fuel cell construction

The single reactant fuel cells, regardless of geometry, are constructed similarly. Here I describe the fabrication procedure in chronological order, summarized graphically in Figure 4.2.1.

I start with a 75 mm by 25 mm clean glass substrate (S17466, Thermo Fisher Scientific, Waltham, MA). (i) The substrate is coated with approximately 4 ml of positive photoresist (Microposit S1813, Shipley Company, Marlborough,

MA), and spun at 4000 rpm for 45 seconds, accelerating the spin at 324 rpm s^{-1}. The resulting thickness is between 0.9 to 1.3 μm according to manufacturer specifications. (ii) The substrate and photoresist are then baked on a hot plate at 150 °C for 35 minutes. (iii) After baking, the substrate is cooled down to room temperature and pressed against with a custom Mylar photomask (Fineline Imaging, Colorado Springs, CO). (iv) The photomask exposes areas on the resist to 22 mW cm^{-2} from an aligner's UV source. (v) After exposure the substrate is manually agitated in a 5:1 v/v ratio of developer (MF-351, Shipley Company) to DI water for approximately one minute, and then rinsed in DI water and dried with nitrogen gas. The development patterns the photoresist and exposes the glass areas to be metal coated. (vi) The substrates are placed inside the chamber of a thermal evaporator (Model 308R, Cressington Scientific Instruments, Watford, UK) with the exposed glass pattern facing a chrome plated tungsten rod (CRW-1, RD Mathis Company, Long Beach, CA) and tungsten boat (ME5-.005W, RD Mathis) holding approximately 0.5 g of gold shot (CAS 7440-57-5, Alfa Aesar, Ward Hill, MA). (vii) The chamber is pumped down to approximately 6E-6 mbar, at which point the input power to the chrome-tungsten rod slowly ramps up to 90 W. The ramping procedure is potentiodynamic and user controlled to ensure even current increase in the tungsten heat source. Chrome deposits at a rate of 1 nm every ten seconds to a total thickness of 15 nm, monitored by a quartz crystal microbalance. The chrome film serves as an adhesion layer for thin metal films which are generally soft. (viii) The power supply is then switched to the gold heat source and gold is evaporated at a similar rate and a power of 180 W to

a film thickness of 65 nm. (ix) The chamber is vented and then each coated substrate is sonicated in an acetone bath for photoresist liftoff. The acetone dissolves the photoresist, leaving behind a gold electrode patterned according to the photomask exposure. (x) The substrates are cleaned with DI water and dried with nitrogen gas. For platinum coating, steps (i) and (ii) above are repeated for the already prepared glass/gold. The mask contact in step (iii) is now critical and done through a microscopic aligner (HTG, ABM, Scotts Valley, CA) to ensure appropriate spacing and no contact between the gold pattern and the new exposure. Steps (iv) and (v) are repeated for the new exposure. For the deposition - steps (vi) through (viii) - a dual head sputter system and vacuum chamber deposits 15 and 65 nm of chrome and platinum respectively. The liftoff procedure and rinsing in steps (ix) and (x) are repeated for the platinum coat. Overall, the procedure results in five glass substrates patterned with gold and platinum electrodes, each separated by a distinct predefined spacing.

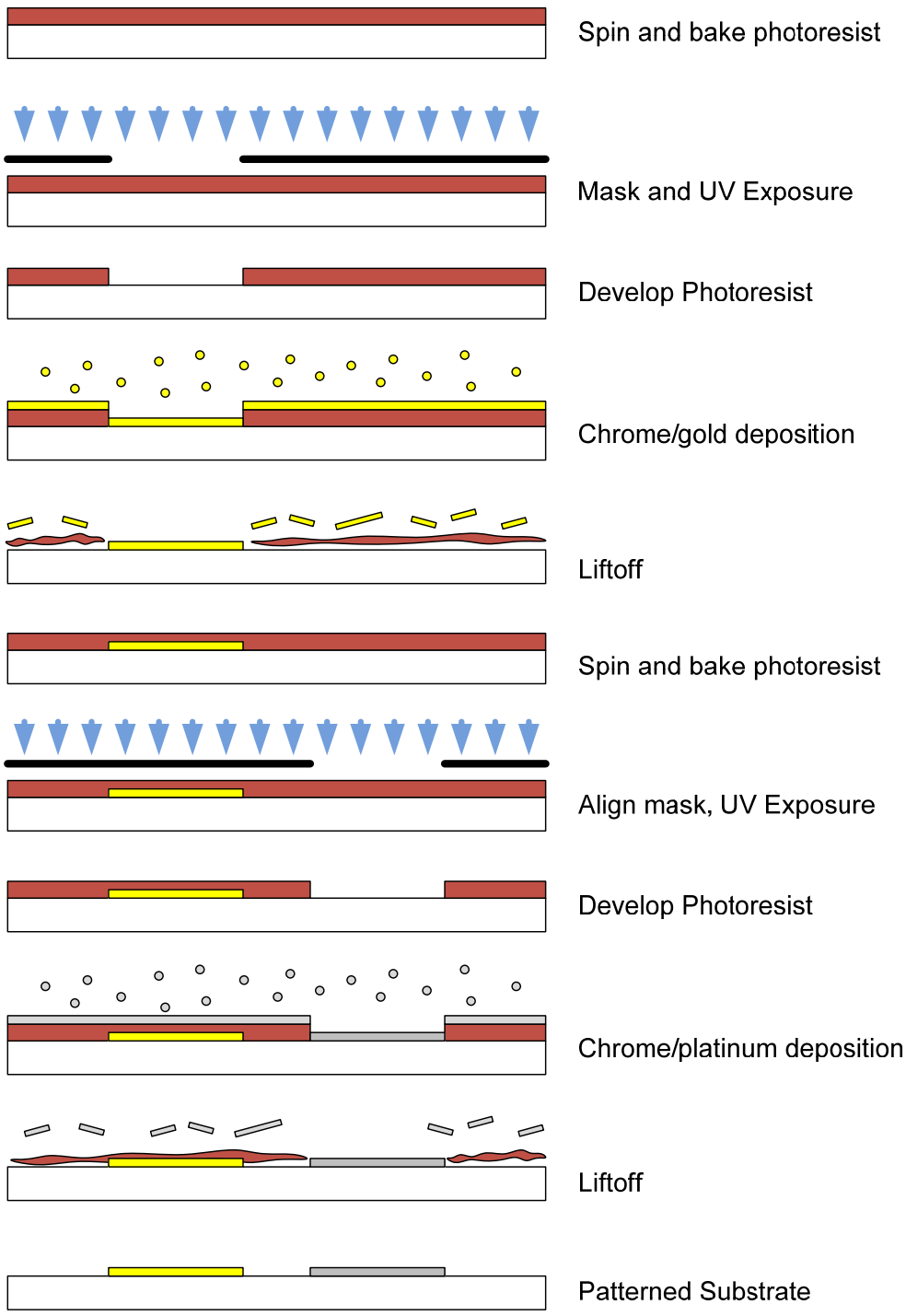

Figure 4.2.1: Photolithography, metal deposition, and liftoff processes for gold and platinum patterning on a glass substrate.

The next step is to create the fluidic channels and ports. All the channels were fabricated by laser ablating double-sided adhesive Mylar (3M), measured at 70 µm thick. The adhesive layer is aligned on the patterned electrode substrate, and then sealed on top with an acrylic layer containing the fluidic ports. Figure 4.2.2 shows an example of each geometric variation. For characterizing the effect of the electrode spacing g, channels of lengths $2L+g$ and width w ($A=wh$, h being the thickness) are adhered to each of the five substrates. L and w are held constant for each electrode gap spacing g. For varying the interfacial area A, four channels of constant length $2L+g$ and increasing width w are adhered to the same substrate. In these two experiments, L and g are aligned in the y direction, and w and the reactant flow are in the x direction. For characterizing the effect of the electrode length L, channels of constant w are adhered to a single substrate (constant g). For the latter experiment, L, g, and the reactant flow are in the y direction, and w remains aligned with the x direction.

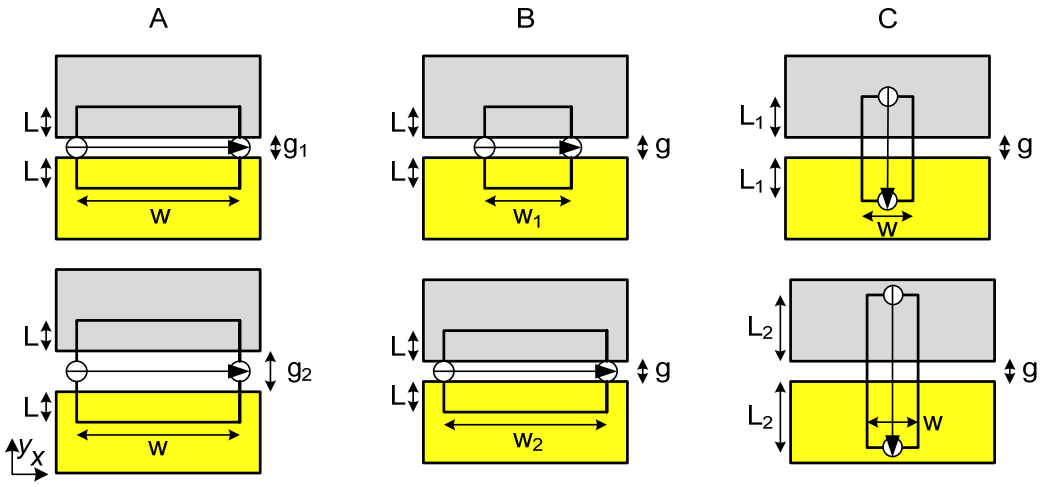

Figure 4.2.2: Single reactant microfluidic fuel cell with varying electrode spacing (A), interfacial area (B), and electrode length (C). Arrows connecting fluidic ports depict flow direction for each case.

The last step is to interface the assembled microfluidic fuel cell fluidically and electrically. Hydrogen peroxide is delivered to the fuel cell via syringe pump (PHD 2000, Harvard Apparatus, Holliston, MA) connected to 1.5 mm tubing (Tygon™ EW-06418-02, Cole Parmer, Vernon Hills, IL) bonded to the ports with quick dry epoxy. Copper foil strips are cut and connected to exposed areas of platinum and gold through a silver based conductive epoxy (Part 8331-14G, MG Chemicals, Canada). Electrochemical polarization is performed potentiostatically (from short circuit to open circuit) through a source meter (Model 6430, Keithley Instruments, Cleveland, OH) connected to a PC via GPIB and Labview.

4.2.2. Chemistry

Hydrogen peroxide (30% v/v, CAS 7722-84-1, Thermo Fisher Scientific) is diluted to 2 % v/v with DI water. At the anode the oxidation reaction

$$H_2O_2 \leftrightarrow 2H^+ + 2e^- + O_2, \tag{4.2.1}$$

occurs and at the cathode the reduction reactions

$$H_2O_2 + 2H^+ + 2e^- \leftrightarrow 2H_2O \tag{4.2.2}$$

and, in the presence of oxygen,

$$\frac{1}{2}O_2 + 2H^+ + 2e^- \leftrightarrow H_2O \tag{4.2.3}$$

occur. Since the same reactant is present at both electrode surfaces the standard reversible potentials are not applicable. Wang et al. report a net open circuit potential of approximately 40 mV for reactions (4.2.1) and (4.2.2) through independent cyclic voltammetry measurements, inferring that the anode and cathode are platinum and gold, respectively [78]. These measurements are in agreement with the results presented in the next section.

4.3. Results and discussion

In this section I present the results from the electrochemical characterization of the fuel cell at the various geometric configurations discussed in the previous section. I also justify the results through appropriate resistive and mass transport scaling laws.

4.3.1. Fuel cell polarization

Figure 4.3.1 compares polarization data for the peroxide fuel cell at different widths between the anode and cathode. In this geometry the gap spacing and electrode length are held constant and the only variation is in the interfacial area A through the width w. The reactant flow rate is 0.5 ml min^{-1} and parallel with w. The short circuit (maximum) current increases with increasing w, primarily due to reducing the Ohmic losses $R=g/\sigma A$ through increasing A. Ohmic losses derived from the polarization curves reflect the apparent resistance – a first degree representation of all three potential losses in the fuel cell – as opposed to the actual in series (resistive) and capacitive (electric double layer induced) impedance of the fuel cell. Figure 4.3.2 plots apparent fuel cell resistance, retrieved from linear fits of each polarization curve, against the corresponding

width. The resistance appears to have an initial sharp decay which levels off as w increases, as primarily expected from the definition of R above. The solid curve in Figure 4.3.2 plots the relationship $R=g/\sigma wh$, where g and h are 45 and 70 μm respectively and σ is 2 μS cm^{-1}, measured by a conductivity meter. This curve represents the Ohmic limit of the fuel cell, i.e. a fuel cell operating with very diminutive mass transport losses. The polarization data has a good initial agreement with the Ohmic scaling, but deviates at subsequent widths by an increase in resistance. The increase in R at larger w is due to the onset of mass transport losses at the electrode surface. In the laminar flow regime and for a reacting flow at a flat boundary, a concentration boundary layer δ_c develops as

$$\delta_c \approx \frac{5w}{Sc^{1/3}Re_w^{1/2}} = \frac{5\sqrt{w}}{Sc^{1/3}\sqrt{\frac{U}{\nu}}}, \tag{4.3.1}$$

where Sc is the Schmidt number, Re is the Reynolds number, U is the average velocity, and v is the kinematic viscosity [82]. The onset of mass transport losses is tantamount to a reactant flux to the surface limited by diffusion. The diffusion limited current density i can then be expressed as

$$i = nFD\nabla C \approx nFD\frac{C - C_s}{\delta_c}, \tag{4.3.2}$$

where n is the number of electrons transferred, F *is* Faraday's constant, D is the diffusion coefficient of the reactant, and C and C_s are respectively the bulk and electrode surface reactant concentration. The total current output I from a pair of electrodes each $w \times h$ in surface area is then

$$I = 2\int_{L}\left(\int_{w} i \cdot dw\right)\cdot dL\,, \tag{4.3.3}$$

Upon integration the current I scales with $\sqrt{w}$. If this is the short circuit current measured through polarization, then an apparent mass-transport based resistance R_m can be expressed as

$$R_m \propto \beta w^{-1/2}\,, \tag{4.3.4}$$

where β is a constant encompassing the potential drop from polarization and all other parameters aside from w in equations (4.3.1) through (4.3.3). The dashed curve in Figure 4.3.2 plots the dependence of R_m on w and compares it to the polarization data and the Ohmic scaling of R. For fitting purposes, the constant β is pinned to the data point at the shortest interfacial width. The mass transport scaling provides a better fit to the data. This suggests that, at a given Peclet number $Pe=Re\times Sc$, the data scales more closely with diffusion limited analysis due to mass transport restrictions at longer interfacial widths.

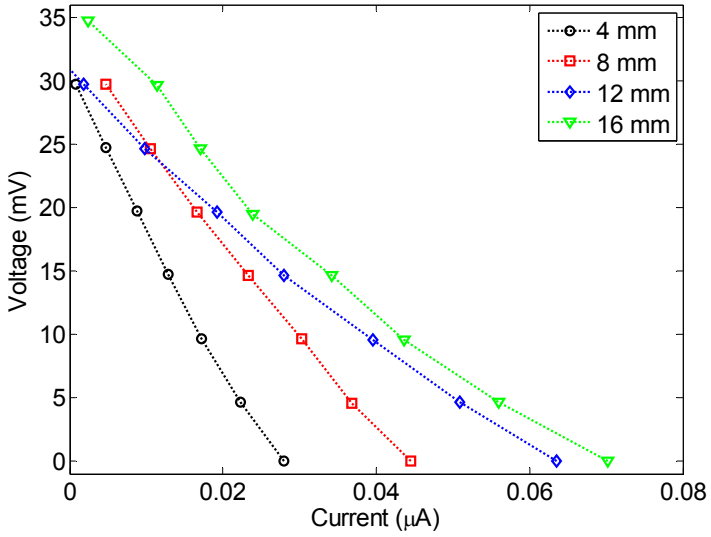

Figure 4.3.1: Polarization curves for the single reactant (2% v/v H_2O_2) membraneless fuel cell at various interfacial lengths between the platinum anode and gold cathode. The cell's height, gap spacing between the electrodes and electrode length are held constant at 70 μm, 45 μm, and 1 mm, respectively. The reactant flow rate is 0.5 ml min^{-1}. Increasing the ionic exchange interfacial area between the electrodes reduces Ohmic losses and results in an increased total current from the fuel cell.

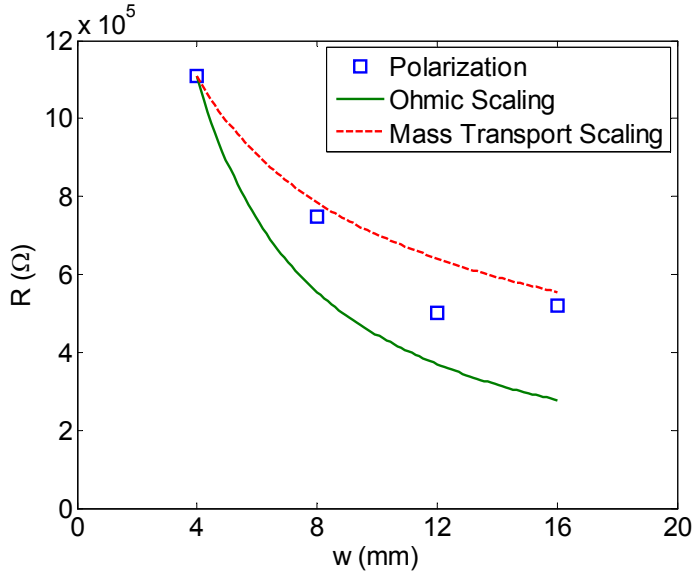

Figure 4.3.2: Comparison of apparent fuel cell resistance values obtained through polarization, and calculated through Ohmic scaling ($R \propto w^{-1}$) and mass transport scaling ($R \propto w^{-1/2}$). The ion exchange area A increases with increasing width w. Apparent resistance increases at larger interfacial areas because downstream boundary layer growth inhibits utilization and thus reduces the maximum current.

Figure 4.3.3 plots the apparent resistance in the fuel cell at various electrode spacing, 0.5 ml min^{-1} flow rate, 1 mm electrode length, and 12 mm electrode width. The resistance increases at larger values of electrode spacing, attributed to increases in Ohmic losses. The solid line in Figure 4.3.3 plots the Ohmic relationship $R=g/\sigma wh$. The polarization data and theoretical relationship correlate well. The error bars in Figure 4.3.3 represent one standard deviation of the measured current, calculated through uncertainty propagation as $\Delta R = \sqrt{|\Delta I|^2 \left(V/I^2\right)^2}$. The error bars increase when the electrode spacing

increases. Hydrogen peroxide undergoes spontaneous decomposition to water and oxygen on platinum, regardless of whether or an electrochemical circuit is established. At larger values of *g*, the electrochemical ion bridge connecting the two half cells is less conductive. Therefore, spontaneous peroxide decomposition at the platinum sites begins to depose the intended oxidation. The decomposition, along with sudden bubble nucleation and detachment from the surface, results in sharp and random gradients in the measured current, which translates to the error shown on Figure 4.3.3.

Figure 4.3.4 compares polarization curves for different electrode lengths of platinum and gold. The length for the anode and cathode increases equally and therefore the ratio of platinum to gold is 1:1 in all cases. The cell's height is 70 μm, the electrode spacing is 45 μm, and the electrode width is 1.35 mm. The reactant flow rate is 0.5 ml min^{-1}. The polarization curves show that increasing electrode length alone has a marginal effect on the short circuit current in the fuel cell. Reaction theory dictates that reactant utilization should scale as e^{-L} [72]. However, the latter scaling is under the assumption that the reaction rate constant is spatially invariant, which is untrue for fuel cells since local Ohmic and mass transport conditions in the reaction domain may alter the current density. In the next sub-section I present a scaling argument that investigates a spatially varying rate constant and its effects on current output.

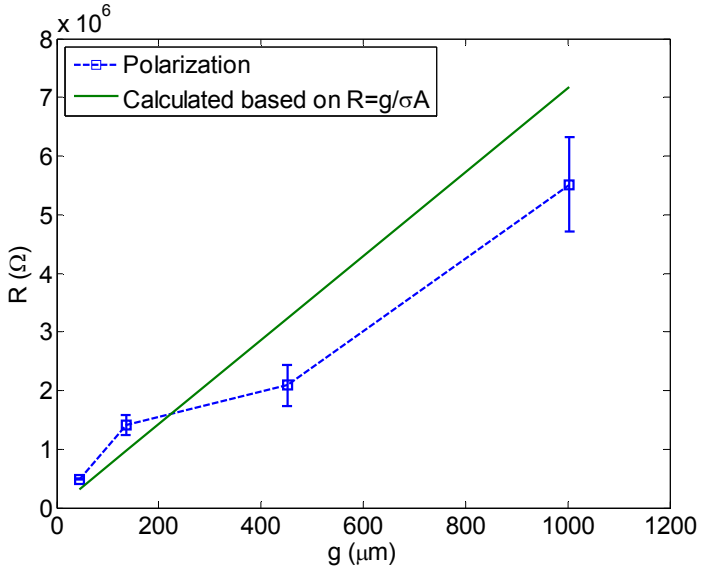

Figure 4.3.3: Apparent (polarization) fuel cell resistance versus the electrode spacing for 2 % v/v peroxide. The flow rate, electrode length, and width were held constant at 0.5 ml min^{-1}, 1 mm, and 12 mm. The data is in good agreement with Ohmic scaling, suggesting small mass transport losses.

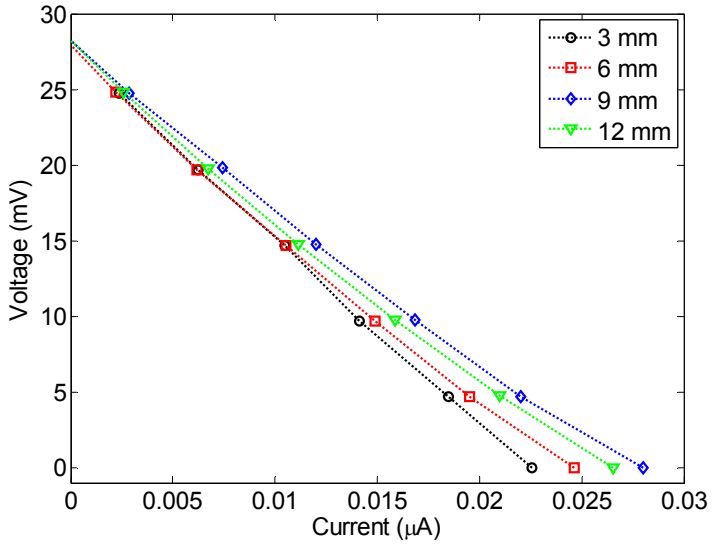

Figure 4.3.4: Polarization curves for the single reactant (2% v/v H_2O_2) membraneless fuel cell at various electrode lengths (1:1 Pt to Au). The cell's height is 70 μm, the electrode spacing is 45 μm, and the electrode width is 1.35 mm. The reactant flow rate is 0.5 ml min^{-1}. At an increased distance from the resistive interface (gap), reactant utilization decreases due to Ohmic losses. Therefore, increasing electrode length alone has negligible effect on maximum current.

4.3.2. One dimensional scaling model

Figure 4.3.5 shows a one dimensional representation of the single reactant microfluidic fuel cell. Reactant with initial concentration C_o and average speed U enter the anodic half cell at x=-a. The electrode spacing between the half cells is for $x \in [-g, g]$ and the reactant exits at x=a. The electrode length is L=a-g.

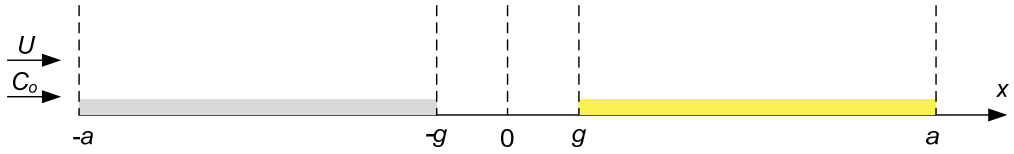

Figure 4.3.5: Diagram illustrating a one dimensional simplification of the single reactant membraneless fuel cell.

Conservation of the inlet, outlet, generation, and steady state accumulation of the molar flow rate is described as

$$F_x - F_{x+\Delta x} + rS(A\Delta x) = 0\,, \tag{4.3.5}$$

where F is the molar rate (mol s^{-1}), r is the heterogeneous reaction rate (mol $m^{-2}s^{-1}$), S is the surface to volume ratio (m^2 m^{-3}), A is the cross-sectional area of a unit depth and height (m^2), and Δx is the infinitesimal width (m). Differentiating equation (4.3.5) at limit $\Delta x \rightarrow 0$ results in the expression

$$-\frac{1}{A}\left(\frac{dF}{dx}\right) + rS = 0\,. \tag{4.3.6}$$

Expressing the molar rate as the sum of the diffusive and convective flux leads to

$$F = \left(-D\frac{dC}{dx} + UC\right)A\,, \tag{4.3.7}$$

where C is the species concentration (mol m^{-3}), D is the diffusion coefficient (m^2 s^{-1}), and U is average fluid velocity through the medium (m s^{-1}).

Substituting equation (4.3.7) into (4.3.6) yields

$$D\frac{d^2C}{dx^2} - U\frac{dC}{dx} + rS = 0\,. \tag{4.3.8}$$

Equation (4.3.8) is the steady state, 1-dimensional advection diffusion equation with volumetric reactions. I define r at the catalyst surface using first order reaction law

$$r = -kC, \tag{4.3.9}$$

Here k is the mass transport coefficient (m s^{-1}), also defined as the heterogeneous reaction rate constant. Rewrite equation (4.3.8) as

$$D\frac{d^2C}{dx^2} - U\frac{dC}{dx} - kSC = 0. \tag{4.3.10}$$

Define C_o and L as the bulk species conservation and characteristic length, respectively. Set $kS=k_h$ and non-dimensionalize equation (4.3.10) using $\phi = C / C_0$ and $\lambda = x / a$ to arrive at

$$\frac{D}{a^2}\frac{d^2\phi}{d\lambda^2} - \frac{U}{a}\frac{d\phi}{d\lambda} - k_h\phi = 0. \tag{4.3.11}$$

Rewrite equation (4.3.11) in terms of the Peclet number $Pe=Ua/D$

$$\frac{1}{Pe}\frac{d^2\phi}{d\lambda^2} - \frac{d\phi}{d\lambda} - \frac{ak_h}{U}\phi = 0, \tag{4.3.12}$$

Assuming that the domain is convection dominant (high Pe), typical of a practical setting, the second order term in equation (4.3.12) scales as $1/Pe$ which leads to the simplification

$$-\frac{d\phi}{d\lambda} - \frac{ak_h}{U}\phi = 0. \tag{4.3.13}$$

Re-dimensionalizing λ in equation (4.3.13) leads to

$$\frac{d\phi}{dx} + \frac{k_h}{U}\phi = 0. \tag{4.3.14}$$

I define a spatially varying rate constant k_h such that $k_h = \kappa / |x|$. The dependence of k_h on x is Ohmic; the further a reaction site is from the gap spacing, the lower in magnitude its rate constant. The constant κ has units of ($\mathrm{m\,s^{-1}}$) and, while without a specific numerical value, depends on Ohmic properties such as the conductivity of the domain and interfacial geometries between the half cells. Define the Damkohler number, $Da \equiv \kappa / U$, and rewrite equation (4.3.14) to

$$\frac{d\phi}{dx} + \frac{Da}{|x|}\phi = 0, \tag{4.3.15}$$

Equation (4.3.15) is solved analytically over the two domains $x \in [-a, g)$ and $x \in [g, a)$. In the domain $x \in [-g, g)$ no reactions are present and thus the equation reduces to $d\phi / dx = 0$. The initial condition for the first domain is $\phi_1(-a) = 1$, for the second domain $\phi_2(-g) = \phi_1(-g)$, and for the third domain $\phi_3(g) = \phi_2(g)$, where the subscripts 1, 2, and 3 correspond to the consecutive domains in x. Integrating equation (4.3.15) and applying the initial conditions leads to

$$\phi_1(x) = \left(\frac{-x}{a}\right)^{Da}, \tag{4.3.16a}$$

$$\phi_2(x) = \left(\frac{g}{a}\right)^{Da}, \tag{4.3.16b}$$

and

$$\phi_3(x) = \left(\frac{g^2}{ax}\right)^{Da}. \tag{4.3.16c}$$

Several plots of $\phi(x)$ are shown in Figures 4.3.6 and 4.3.7. In all cases the *Da* number is 0.05, selected according to a typical reaction speed of 5×10^{-5} m s^{-1}, and an average velocity of 10^{-3} m s^{-1}. At a constant *Da*, all of the plots are governed by similar trends regardless of the geometry. The dimensionless concentration gradually decreases at the channel entrance, and as the electrode gap approaches the concentration decrease becomes more significant. The concentration remains constant in the gap since the reactant simply undergoes convection in the spacing. A sharp drop in concentration occurs at the inlet of the second half cell, followed by a slower decay as the reactant moves away from the gap spacing. Figure 4.3.6 investigates the behavior of $\phi(x)$ at constant electrode length and varying gap spacing. The exit concentration decreases as *g* decreases. Therefore, reactant utilization increases with shorter electrode gaps. Increasing reactant utilization results in higher output currents, which is reflected as lower apparent resistances in the fuel cell polarization. Experimental data presented in Figure 4.3.3 agrees with this scaling model in that the electrode spacing largely influences the electrochemical polarization of the fuel cell. Figure 4.3.7 shows $\phi(x)$ at constant gap length and varying electrode length. The exit concentration decreases with longer electrodes since the fuel is subjected to extended reactions. However, further increases in electrode lengths lead to an asymptoting behavior in reactant utilization. The reaction rates scale inversely with increasing distance from the electrode spacing, and therefore extending the electrodes away from the gap will yield marginal current output, and therefore power. This phenomenon is also demonstrated experimentally as shown previously in Figure 4.3.4.

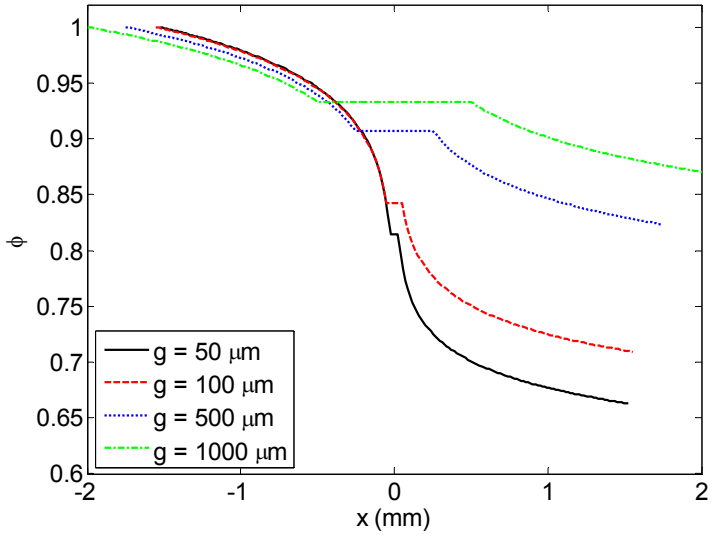

Figure 4.3.6: Plots of $\phi(x)$ at constant electrode length and varying gap length. Da=0.05.

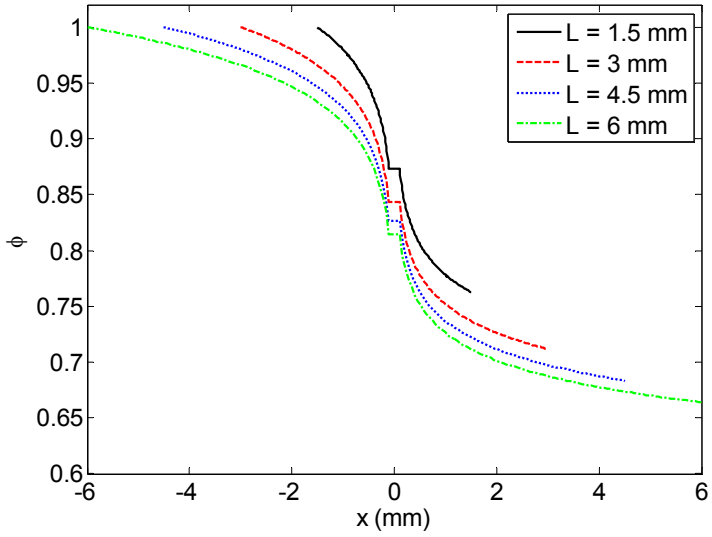

Figure 4.3.7: Plots of $\phi(x)$ at constant gap length and varying electrode length. Da=0.05.

It is important to note that the abovementioned model and experiments were in accordance given the geometric relationship $g<L$. To examine the scaling model's behavior at any geometry, define a dimensionless total current converted from the fuel cell in Figure 4.3.5 as the summation of individual flux terms at each x location,

$$\Gamma \equiv \int_{-a}^{-g} \frac{1}{|x|} \times \left(1-\phi_1(x)\right) dx + \int_{-g}^{g} 0 \times \left(1-\phi_2(x)\right) dx + \int_{g}^{a} \frac{1}{|x|} \times \left(1-\phi_3(x)\right) dx \,. \tag{4.3.17}$$

Performing the integration for $a=g+L$ leads to

$$\Gamma = 2\ln\left(\frac{g+L}{g}\right) + \frac{1}{Da}\left(\left(\frac{g}{g+L}\right)^{2Da} - 1\right). \tag{4.3.18}$$

Figure 4.3.8 shows a contour plot of Γ as a function of g and L. For comparison with the previous observations, the gradients of Γ with respect to g are sharper than those with respect to L when $g<L$. This is consistent with the previous findings which state that decreasing electrode spacing has more significant effects on total current increase, when compared to increasing electrode length. At equal gap and electrode lengths the gradients are equal. When $L<g$, the gradients of Γ with respect to L become sharper than those with respect to g. While the two latter geometries are not available experimentally, Figure 4.3.8 suggests that designing the fuel cell with the constraints $g<L$ and $\frac{\partial \Gamma}{\partial L} \to 0$ (i.e. moving towards the northwest portion of the contour plot) increases output currents and reduces the required electrode areas.

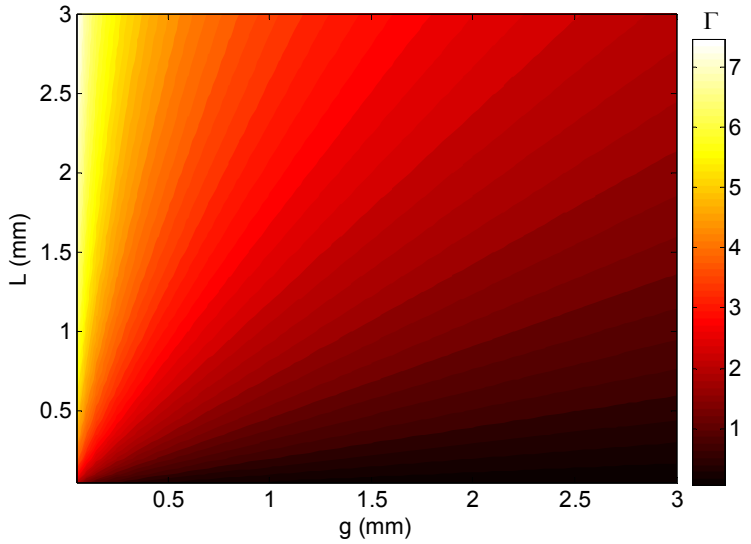

Figure 4.3.8: Contour plot of the dimensionless current extracted from the one dimensional single reactant fuel cell model versus electrode length and electrode spacing. Larger currents are possible by decreasing *g* and optimizing *L*.

4.4. Conclusions

Membraneless microfluidic fuel cells have a tight coupling between their mass transport and electrical features since their ion exchange medium is fluidic. The majority of published work on microfluidic fuel cells has been to introduce new flow geometries and chemistry, and to date very little experimental work details geometric variations. I present a series of microfluidic membraneless fuel cells that use hydrogen peroxide as a single reactant on a gold cathode and platinum anode. These fuel cells differ only in their interfacial width, electrode spacing, and electrode lengths. Increasing the interfacial width increases the ionic exchange area between anode and cathode and hence reduces Ohmic losses in the fuel cell. However, at elongated flow geometries concentration boundary layers

become thicker, inducing mass transport losses in the fuel cell if the *Pe* number is not corrected for the new geometry. Decreasing the electrode spacing also reduces Ohmic losses. Increasing the electrode length increases reactant utilization which is perceived as an Ohmic enhancement from polarization; however this increase is not long-lasting for constant electrode spacing and should therefore be optimized according to design criteria. The experimental trends agree with those obtained through an Ohmic-scaled model of a membraneless fuel cell.

CHAPTER 5

Summary and Contributions

5.1. Background and significance

The rapid advancement of portable electronic devices has significantly increased their power demands. Current state of the art battery technologies are a major contributor to the overall weight and size of the portable system due to their low energy densities. Liquid and gaseous fuels exhibit higher energy densities compared to battery systems, and offer greater flexibility in their storage, handling, and system implementation. Miniaturized polymer membrane fuel cells that use such fuels present a small scale and portable solution with high fuel conversion efficiency. However, like their full scale counterparts, miniaturized fuel cells suffer from complications with membrane durability and catalyst flooding. These challenges increase the overall cost and maintenance, and reduce the system's reliability.

More recently, micron scale liquid fuel cells have been developed as alternative portable sources. Microfluidic fuel cells avoid the use of a semi-permeable membrane by leveraging laminar interfaces between the liquid streams to separate the reactants. Microfluidic fuel cells have primarily relied on parallel flowing laminar streams of fuel and oxidant. The reactants' electrodes are located along opposite sidewalls of the microfluidic channel. In the parallel flow design, higher flow rates yield higher power output, but at the expense of reduced fuel utilization because the reactants are advected downstream before they can react. Lower reactant flow rates increase fuel conversion, but waste reactants because of

increased diffusive mixing between the two streams and have lower power density because of thick concentration boundary layer at the electrodes.

5.2. Research objectives

The goal of my research is to design and characterize a microfluidic fuel cell that exhibits high power density and high fuel utilization. To achieve this goal, I divide the research into two phases. In the first phase of this work, I present membraneless microfluidic fuel cell architectures that utilize porous electrodes, and interface reactants along concise zones to reduce diffusive mixing. Porous electrodes increase the reaction surface area and reduce the concentration boundary layer thickness, which result in increased power output. Reducing the diffusive mixing between the two streams reduces both reactant depletion and the undesirable potential losses associated with the presence of a reactant at its counter electrode. I investigate the effects of reactant flow rates, supporting electrolyte concentrations, and electrolyte flow rates on the fuel cell polarization.

The second phase of this work presents experiments aimed at understanding the influence of geometric variations on the fuel cell's power output and fuel utilization. The distance between the two electrodes, the lengths of the electrodes, and the cross sectional area of the ionic interface are varied to investigate their effect on fuel cell power and fuel utilization. To do this, I present a membraneless fuel cell that relies on the electrochemical behavior of hydrogen peroxide, as a single reactant, on two different metal surfaces. The motivation behind a single reactant scheme is to provide a controlled experimental platform where flow field perturbations are reduced.

5.3. Research summary

Higher flow rates in microfluidic fuel cells result in higher power densities attributed to enhanced mass transport due to thinner concentration boundary layers at the electrode surface. Higher flow rates however reduce the fuel utilization since reactants are advected to the outlets prior to their reaction faster. Higher electrolyte conductivities reduce the Ohmic losses in the cell and increase power output. Shortening the extended interface, typical in parallel flow regimes, reduces the diffusive mixing between the reactants. Also, extending the shortened interface in directions that are not along the flow streamlines, or increasing the interface instances increases the ionic exchange area which increases current density at any potential. This increases both thermodynamic and Faradaic efficiencies in the fuel cell. Using porous electrodes increases reactant's exposure to the electrode surface area and increases the fuel utilization. Reducing the gap between the electrodes and increasing the cross sectional area between the two electrodes decreases the Ohmic associated losses in the fuel cell. Increasing the electrode length increases reactant utilization which is perceived as an Ohmic enhancement from polarization; however this increase is not long-lasting for constant electrode spacing and should therefore be optimized according to design criteria

5.4. Research impact

Successful integration of the completed research will enable development of high energy and power density portable power sources that are safe, robust, and require little maintenance. Potential applications include powering cell phones,

portable computers, handheld global positioning systems, and unmanned small scale military devices. The novel microfluidic fuel cell architectures use unique flow patterns with porous electrodes to provide high power densities without sacrificing fuel utilization. Experiments using the single reactant fuel cell are aimed to understand the role of geometric parameters on the fuel cell performance so that production and commercial designs may be optimized for maximum power.

5.5. Contributions

Contributions to the scientific community include three published articles to the Journal of Power Sources on the radial sequential flow fuel cell, counter flow fuel cell, and multi-pass fuel cell. A current manuscript on the role of fuel cell geometry is being prepared for submission accordingly. The novelty and potential commercial value of this work is demonstrated in several patent applications and intellectual property disclosures.

REFERENCES

[1] D. Dunn-Rankin, E.M. Leal, D.C. Walther, Progress in Energy and Combustion Science, 31 (2005) 422-465.

[2] C.K. Dyer, Journal of Power Sources, 106 (2002) 31-34.

[3] J. Larminie, A. Dicks, Fuel Cell Systems Explained, 2nd ed., John Wiley & Sons Ltd, 2003.

[4] A. Collier, H.J. Wang, X.Z. Yuan, J.J. Zhang, D.P. Wilkinson, International Journal of Hydrogen Energy, 31 (2006) 1838-1854.

[5] F.A. de Bruijn, V.A.T. Dam, G.J.M. Janssen, Fuel Cells, 8 (2008) 3-22.

[6] D.A. Schiraldi, Polymer Reviews, 46 (2006) 315-327.

[7] W. Schmittinger, A. Vahidi, Journal of Power Sources, 180 (2008) 1-14.

[8] H.L. Tang, P.K. Shen, S.P. Jiang, W. Fang, P. Mu, Journal of Power Sources, 170 (2007) 85-92.

[9] J. Wu, X.Z. Yuan, J.J. Martin, H. Wang, J. Zhang, J. Shen, S. Wu, W. Merida, Journal of Power Sources, 184 (2008) 104-119.

[10] C.R. Buie, J.D. Posner, T. Fabian, C.A. Suk-Won, D. Kim, F.B. Prinz, J.K. Eaton, J.G. Santiago, Journal of Power Sources, 161 (2006) 191-202.

[11] K.D. Hristovski, B. Dhanasekaran, J.E. Tibaquira, J.D. Posner, P.K. Westerhoff, Journal of Water Supply Research and Technology-Aqua, 58 (2009) 327-335.

[12] H. Li, Y.H. Tang, Z.W. Wang, Z. Shi, S.H. Wu, D.T. Song, J.L. Zhang, K. Fatih, J.J. Zhang, H.J. Wang, Z.S. Liu, R. Abouatallah, A. Mazza, Journal of Power Sources, 178 (2008) 103-117.

[13] N. Yousfi-Steiner, P. Moçotéguy, D. Candusso, D. Hissel, Journal of Power Sources, 194 (2009) 130-145.

[14] J.R. Yu, T. Matsuura, Y. Yoshikawa, M.N. Islam, M. Hori, Physical Chemistry Chemical Physics, 7 (2005) 373-378.

[15] X. Cheng, J.L. Zhang, Y.H. Tang, C.J. Song, J. Shen, D.T. Song, J.J. Zhang, Journal of Power Sources, 167 (2007) 25-31.

[16] K.J. Jeong, C.A. Miesse, J.H. Choi, J. Lee, J. Han, S.P. Yoon, S.W. Nam, T.H. Lim, T.G. Lee, Journal of Power Sources, 168 (2007) 119-125.

[17] S.S. Kocha, J.D.L. Yang, J.S. Yi, Aiche Journal, 52 (2006) 1916-1925.

[18] J.D. Morse, International Journal of Energy Research, 31 (2007) 576-602.

[19] A. Kundu, J.H. Jang, J.H. Gil, C.R. Jung, H.R. Lee, S.H. Kim, B. Ku, Y.S. Oh, Journal of Power Sources, 170 (2007) 67-78.

[20] S. Ha, B. Adams, R.I. Masel, Journal of Power Sources, 128 (2004) 119-124.

[21] C. Rice, R.I. Ha, R.I. Masel, P. Waszczuk, A. Wieckowski, T. Barnard, Journal of Power Sources, 111 (2002) 83-89.

[22] Y.Q. Jiang, X.H. Wang, L.Y. Zhong, L.T. Liu, Journal of Micromechanics and Microengineering, 16 (2006) S233-S239.

[23] J. Yeom, G.Z. Mozsgai, B.R. Flachsbart, E.R. Choban, A. Asthana, M.A. Shannon, R. Kenis, Sensors and Actuators B-Chemical, 107 (2005) 882-891.

[24] A. Kamitani, S. Morishita, H. Kotaki, S. Arscott, Journal of Micromechanics and Microengineering, 18 (2008).

[25] S.C. Yao, X.D. Tang, C.C. Hsieh, Y. Alyousef, M. Vladimer, G.K. Fedder, C.H. Amon, Energy, 31 (2006) 636-649.

[26] H.A. Stone, A.D. Stroock, A. Ajdari, Annual Review of Fluid Mechanics, 36 (2004) 381-411.

[27] T. Thorsen, S.J. Maerkl, S.R. Quake, Science, 298 (2002) 580-584.

[28] G.M. Whitesides, Nature, 442 (2006) 368-373.

[29] G.M. Whitesides, A.D. Stroock, Physics Today, 54 (2001) 42-48.

[30] S.H. Fogler, Elements of Chemical Reaction Engineering, Prentice Hall, Inc., Englewood Cliffs, NJ., 1986.

[31] M. Brivio, W. Verboom, D.N. Reinhoudt, Lab on a Chip, 6 (2006) 329-344.

[32] R. Ferrigno, A.D. Stroock, T.D. Clark, M. Mayer, G.M. Whitesides, Journal of the American Chemical Society, 124 (2002) 12930-12931.

[33] E.R. Choban, L.J. Markoski, A. Wieckowski, P.J.A. Kenis, Journal of Power Sources, 128 (2004) 54-60.

[34] R.F. Ismagilov, A.D. Stroock, P.J.A. Kenis, G. Whitesides, H.A. Stone, Applied Physics Letters, 76 (2000) 2376-2378.

[35] E. Kjeang, N. Djilali, D. Sinton, T.S. Zhao, Advances in Microfluidic Fuel Cells, in: Micro Fuel Cells, Academic Press, Boston, 2009, pp. 99-139.

[36] E. Kjeang, J. McKechnie, D. Sinton, N. Djilali, Journal of Power Sources, 168 (2007) 379-390.

[37] E. Kjeang, B.T. Proctor, A.G. Brolo, D.A. Harrington, N. Djilali, D. Sinton, Electrochimica Acta, 52 (2007) 4942-4946.

[38] E. Kjeang, R. Michel, D.A. Harrington, N. Djilali, D. Sinton, Journal of the American Chemical Society, 130 (2008) 4000-4006.

[39] K.S. Salloum, J.R. Hayes, C.A. Friesen, J.D. Posner, Journal of Power Sources, 180 (2008) 243-252.

[40] J.L. Cohen, D.J. Volpe, D.A. Westly, A. Pechenik, H.D. Abruna, Langmuir, 21 (2005) 3544-3550.

[41] M.H. Sun, G.V. Casquillas, S.S. Guo, J. Shi, H. Ji, Q. Ouyang, Y. Chen, Microelectronic Engineering, 84 (2007) 1182-1185.

[42] J.R. Hayes, A.M. Engstrom, C. Friesen, Journal of Power Sources, 183 (2008) 257-259.

[43] S.M. Mitrovski, R.G. Nuzzo, Lab on a Chip, 6 (2006) 353-361.

[44] R.S. Jayashree, M. Mitchell, D. Natarajan, L.J. Markoski, P.J.A. Kenis, Langmuir, 23 (2007) 6871-6874.

[45] E. Kjeang, A.G. Brolo, D.A. Harrington, N. Djilali, D. Sinton, Journal of the Electrochemical Society, 154 (2007) B1220-B1226.

[46] A. Lam, D.P. Wilkinson, J.J. Zhang, Journal of Power Sources, 194 (2009) 991-996.

[47] I.B. Sprague, P. Dutta, S. Ha, Proceedings of the Institution of Mechanical Engineers Part a-Journal of Power and Energy, 223 (2009) 799-808.

[48] S. Topcagic, S.D. Minteer, Electrochimica Acta, 51 (2006) 2168-2172.

[49] J. Ma, Y. Liu, Y. Liu, Y. Yan, P. Zhang, Fuel Cells, 8 (2008) 394-398.

[50] F.R. Brushett, R.S. Jayashree, W.-P. Zhou, P.J.A. Kenis, Electrochimica Acta, 54 (2009) 7099-7105.

[51] F.R. Brushett, W.P. Zhou, R.S. Jayashree, P.J.A. Kenis, Journal of the Electrochemical Society, 156 (2009) B565-B571.

[52] E. Kjeang, R. Michel, D.A. Harrington, D. Sinton, N. Djilali, Electrochimica Acta, 54 (2008) 698-705.

[53] E.R. Choban, J.S. Spendelow, L. Gancs, A. Wieckowski, P.J.A. Kenis, Electrochimica Acta, 50 (2005) 5390-5398.

[54] G.H. Miley, N. Luo, J. Mather, R. Burton, G. Hawkins, L.F. Gu, E. Byrd, R. Gimlin, P.J. Shrestha, G. Benavides, J. Laystrom, D. Carroll, Journal of Power Sources, 165 (2007) 509-516.

[55] E. Kjeang, N. Djilali, D. Sinton, Journal of Power Sources, 186 (2009) 353-369.

[56] R.F. Probstein, Physicochemical Hydrodynamics: An Introduction, 2 ed., Wiley, 2003.

[57] F.M. White, Viscous Fluid Flow, McGraw Hill, 2006.

[58] R.B. Bird, E.N. Lightfoot, W.E. Stewart, Transport Phenomena, 2nd ed., John Wiley and Sons, Inc., New York, NY, 2001.

[59] K.S. Salloum, J.D. Posner, Journal of Power Sources, 195 (2010) 6941-6944.

[60] K.S. Salloum, J.D. Posner, Journal of Power Sources, 196 (2011) 1229-1234.

[61] R.J. Adrian, Experiments in Fluids, 39 (2005) 159-169.

[62] J.G. Santiago, S.T. Wereley, C.D. Meinhart, D.J. Beebe, R.J. Adrian, Experiments in Fluids, 25 (1998) 316-319.

[63] D.R. Lide, Ed., CRC Handbook of Chemistry and Physics (Internet Version 2010) 90th ed., CRC Press/Taylor and Francis, Boca Raton, FL.

[64] F.A. Cotton, G. Wilkinson, Advanced Inorganic Chemistry, 4th ed., John Wiley & Sons, 1980.

[65] J.S. Bendat, A.G. Piersol, Random Data: Analysis & Measurement Procedures, John Wiley & Sons, 2000.

[66] A. Bazylak, D. Sinton, N. Djilali, Journal of Power Sources, 143 (2005) 57-66.

[67] F.L. Chen, M.H. Chang, M.K. Lin, Electrochimica Acta, 52 (2007) 2506-2514.

[68] A.S. Hollinger, R.J. Maloney, R.S. Jayashree, D. Natarajan, L.J. Markoski, P.J.A. Kenis, Journal of Power Sources, 195 (2010) 3523-3528.

[69] M. Skyllaskazacos, D. Kasherman, D.R. Hong, M. Kazacos, Journal of Power Sources, 35 (1991) 399-404.

[70] A.C. Burt, I.B. Celik, R.S. Gemmen, A.V. Smirnov, Journal of Power Sources, 126 (2004) 76-87.

[71] T. Mennola, M. Mikkola, M. Noponen, T. Hottinen, P. Lund, Journal of Power Sources, 112 (2002) 261-272.

[72] H.S. Fogler, Elements of Chemical Reaction Engineering, Prentice-Hall, Inc., 1986.

[73] R.S. Jayashree, S.K. Yoon, F.R. Brushett, P.O. Lopez-Montesinos, D. Natarajan, L.J. Markoski, P.J.A. Kenis, Journal of Power Sources, 195 (2010) 3569-3578.

[74] H.B. Park, D.H. Ahmed, K.H. Lee, H.J. Sung, Electrochimica Acta, 54 (2009) 4416-4425.

[75] A. Ebrahimi Khabbazi, A.J. Richards, M. Hoorfar, Journal of Power Sources, 195 (2010) 8141-8151.

[76] I.B. Sprague, D. Byun, P. Dutta, Electrochimica Acta, In Press, Corrected Proof.

[77] B.H. Liu, Z.P. Li, K. Arai, S. Suda, Electrochimica Acta, 50 (2005) 3719-3725.

[78] Y. Wang, R.M. Hernandez, Bartlett, Jr., J.M. Bingham, T.R. Kline, A. Sen, T.E. Mallouk, LANGMUIR, 22 (2006) 10451-10456.

[79] W.F. Paxton, K.C. Kistler, C.C. Olmeda, A. Sen, S.K. St Angelo, Y.Y. Cao, T.E. Mallouk, P.E. Lammert, V.H. Crespi, JOURNAL OF THE AMERICAN CHEMICAL SOCIETY, 126 (2004) 13424-13431.

[80] P. Calvo-Marzal, K.M. Manesh, D. Kagan, S. Balasubramanian, M. Cardona, G.-U. Flechsig, J. Posner, J. Wang, Chemical Communications, (2009).

[81] J.L. Moran, P.M. Wheat, J.D. Posner, PHYSICAL REVIEW E, 81 (2010).

[82] F.P. Incropera, D.P. DeWitt, Fundamentals of Heat and Mass Transfer, 6th ed., John Wiley and Sons, Inc., New York, NY, 2007.